©ESO 2019

Hot WHIM counterparts of FUV O VI absorbers:
Evidence in the line-of-sight towards quasar 3C 273

Jussi Ahoranta[1,2], Jukka Nevalainen[3], Nastasha Wijers[4], Alexis Finoguenov[1], Massimiliano Bonamente[2,5], Elmo Tempel[3,6], Evan Tilton[7], Joop Schaye[4], Jelle Kaastra[4,8], and Ghassem Gozaliasl[9,1]

[1] Department of Physics, University of Helsinki, P.O. Box 64, FI-00014, Finland
[2] Department of Physics, University of Alabama in Huntsville, Huntsville, AL, USA
[3] Tartu Observatory, University of Tartu, Observatooriumi 1, 61602 Tõravere, Estonia
[4] Leiden Observatory, Leiden University, PO Box 9513, NL-2300 RA Leiden, the Netherlands
[5] NASA National Space Science and Technology Center, Huntsville, AL, USA
[6] Leibniz-Institut für Astrophysik Potsdam (AIP), An der Sternwarte 16, D-14482 Potsdam, Germany
[7] Deparment of Physics & Astronomy, Regis University, Denver, CO 80221, USA
[8] SRON Netherlands Institute for Space Research, Sorbonnelaan 2, 3584 CA Utrecht, The Netherlands
[9] Finnish centre for Astronomy with ESO (FINCA), Quantum, Vesilinnantie 5, University of Turku, FI-20014 Turku, Finland

ABSTRACT

Aims. We explore the high spectral resolution X-ray data towards the quasar 3C 273 to search for signals of hot ($\sim 10^{6-7}$ K) X-ray-absorbing gas co-located with two established intergalactic FUV O VI absorbers.
Methods. We analyze the soft X-ray band grating data of all XMM-*Newton* and *Chandra* instruments to search for the hot phase absorption lines at the FUV predicted redshifts. The viability of potential line detections is examined by adopting the constraints of a physically justified absorption model. The WHIM hypothesis is investigated with a complementary 3D galaxy distribution analysis and by detailed comparison of the measurement results to the WHIM properties in the EAGLE cosmological, hydrodynamical simulation.
Results. At one of the examined FUV redshifts, $z = 0.09017 \pm 0.00003$, we measured signals of two hot ion species, O VIII and Ne IX, with a 3.9σ combined significance level. While the absorption signal is only marginally detected in individual co-added spectra, considering the line features in all instruments collectively and assuming collisional equilibrium for absorbing gas, we were able to constrain the temperature ($kT = 0.26 \pm 0.03$ keV) and the column density ($N_{\rm H} \times {\rm Z}_\odot/{\rm Z} = 1.3^{+0.6}_{-0.5} \times 10^{19}$ cm^{-2}) of the absorber. Thermal analysis indicates that FUV and X-ray absorption relate to different phases, with estimated temperatures, $T_{\rm FUV} \approx 3 \times 10^5$, and, $T_{\rm X-ray} \approx 3 \times 10^6$ K. These temperatures match the EAGLE predictions for WHIM at the FUV/X-ray measured $N_{\rm ion}$-ranges. We detected a large scale galactic filament crossing the sight-line at the redshift of the absorption, linking the absorption to this structure.
Conclusions. This study provides observational insights into co-existing warm and hot gas within a WHIM filament and estimates the ratio of the hot and warm phases. Because the hot phase is thermally distinct from the O VI gas, the estimated baryon content of the absorber is increased, conveying the promise of X-ray follow-up studies of FUV detected WHIM in refining the picture of the missing baryons.

Key words. X-rays: Individuals: 3C 273 - Intergalactic medium - Large-scale structure of Universe

1. Introduction

The missing baryons problem (Persic & Salucci 1992) in the low-z universe is likely a manifestation of the limitations of current observational capabilities at the high-energy end of the electromagnetic spectrum. The majority of the non-detected baryons are expected to reside in the warm-hot intergalactic medium (WHIM), the shock-heated diffuse gas accumulated within the large scale structures of dark matter in the Universe (Cen & Ostriker 1999; Davé et al. 1999). Such concentrations of hot, highly-ionized gas are, in principle, observable in the FUV and X-ray bands. Whereas in the FUV band, measurements of broad Lyα and O VI absorption lines in the local ($z < 1$) universe have revealed the warm part ($T \sim 10^{5-6}$ K) of the WHIM (e.g., Tripp et al. 2000), the number of X-ray observations of the hot WHIM phase remains limited. The low expected column densities ($\lesssim 10^{16}$ cm^{-2}) of the most prominent ions in the hot WHIM temperature range ($\sim 10^{6-7}$ K), such as O VII-VIII, Ne IX-X and N VII (e.g., Fang et al. 2002; Wijers et al. 2019), significantly limit the possibilities for studying the hot WHIM with observations using the present instrumentation.

Currently, the method with the most potential for the direct detection of the WHIM uses quasar or blazar emission as a backlight against which absorption signatures might be found. In the FUV band this approach has been successfully applied (e.g., Tripp et al. 2000; Sembach et al. 2001; Williger et al. 2010; Tilton et al. 2012; Shull et al. 2012; Danforth et al. 2016), in contrast to the X-ray band where the observational evidence is typically less solid and therefore subject to other interpretations (see, e.g., discussions in Rasmussen et al. 2007, Bonamente et al. 2017). Present high-energy resolution soft X-ray band instruments' (the XMM-*Newton* RGS and *Chandra* LETG grating spectrometers) effective areas vary from a few to few tens of cm^2 at the relevant energies, and consequently $\sim$ Ms exposure times are typically required to attain sufficient photon statistics for possible WHIM line detections. In such observations, systematics such as instrument calibration uncertainties require special

attention. In recent years, numerous studies of hot WHIM absorbers have been published, for example by Buote et al. (2009), Nicastro et al. (2010), Ren et al. (2014), Bonamente et al. (2016), Nicastro et al. (2018), and Kovacs et al. (2019), among others. However, the number and the significance of the possible hot WHIM detections has remained low, and the fundamental problem remains: about one third of the local baryons remain missing (e.g., Shull et al. 2012; Nicastro et al. 2017).

Future instruments, in particular, the Athena X-IFU (Barret et al. 2016; Kaastra et al. 2013), are targeted at increasing the prospects to measure weak signals from hot WHIM. With that regard, in this work we aim to improve the observational status of hot WHIM absorption under the hypothesis that the warm phase ($T \sim 10^5$ K, well-detected in FUV) of the WHIM is spatially co-located with the hot (10^{6-7} K) WHIM (see Nevalainen et al. 2019 for more discussion). Other authors have previously investigated such an approach. For instance, Yao et al. (2009) stacked the then available ACIS data of several AGN in order to detect possible hot counterparts to the FUV-detected O vi absorbers. Nevalainen et al. (2019) used all available *Chandra* ACIS and XMM-*Newton* RGS data to look for O vii and O viii absorption at FUV-detected redshifts in the sight-line towards PKS2155-304. Neither study detected statistically-significant absorption, instead setting upper limits of $10^{14.5-15.5}$ cm^{-2} of the column densities of the two ions.

In this study, we investigate the sight-line towards the quasar 3C 273 ($z \approx 0.158$, Schmidt 1963), also included in the Yao et al. (2009) sample. This sight-line was chosen because of the exceptionally good photon statistics available for high resolution X-ray spectroscopy. In addition, as we list in Table 1, FUV measurements have detected O vi and broad (> 40 km s^{-1}) Lyman-alpha (BLA) absorption lines at several non-zero redshifts in this sight-line (e.g., Sembach et al. 2001; Williger et al. 2010; Tilton et al. 2012; Danforth et al. 2016). We utilize all the currently available ACIS and RGS data in our analysis (total exposure time > Ms) so that for a single AGN we reach a similar level of sensitivity as the stacked Yao et al. (2009) sample. This enables us to avoid possible problems with stacking data from different instruments, redshifts and targets, therefore improving constraints on potentially co-located warm and hot WHIM gas.

Considering the presumed parameter space of the WHIM (i.e., n_H, Z, T, etc.), it is not expected that photo-ionization by itself would produce high enough amounts of O vii or O viii to be detectable with current X-ray instruments (e.g., Wijers et al. 2019). Since only collisional ionization seems capable of producing high enough ion column densities, in this study we adopt the assumption that collisional ionization equilibrium (CIE) describes the physical state of hot WHIM gas.

The search for the X-ray absorbing gas is conducted at the exact redshifts where significant detections of O vi absorption have been in obtained in the FUV. Although other authors have also used Ne viii as a tracer of hot gas (e.g., Burchett et al. 2019; see also Wijers et al. 2019), the spectral data toward 3C 273 lack the necessary wavelength coverage for such an analysis, so we do not consider it in this analysis. After the initial search for the hot phase absorption lines at the O vi absorber redshifts, each tentative line detection is critically considered by: 1) confirming the signal is consistent between all the measuring instruments, 2) checking the spectral band at the location of potential line detections against possible spectral and co-adding artifacts, and 3) comparing the freely fitted line intensity ratios to the constraints set by the CIE model.

We complement the X-ray analysis with an optical study of the galactic filaments at the location of the absorbers, since large scale filaments are expected to harbor a major fraction of the local missing hot baryons. Finally, we compare our results to the WHIM observables predictions of the EAGLE (Schaye et al. 2015) cosmological, hydrodynamical simulations.

2. Observational X-ray data set

The absorption signatures of the hot WHIM filaments are expected to be close to or beyond the limits of detectability with the current high spectral resolution X-ray instruments. With this in mind, we analyzed all the long exposure ($\gtrsim 20$ ks) 3C 273 observations (as available on Jan 2019) from the XMM-*Newton* RGS (first and second spectral orders), *Chandra* LETG (HRC and ACIS first-order), and *Chandra* MEG (ACIS first-order) instruments. The total RGS exposure times are ≈ 700 ks per instrument, which is substantially longer than that of the *Chandra* instruments (see Table 2).

Due to the shorter observation times and smaller effective area of the *Chandra* instruments as compared to the RGS, the statistical weight of LETG and MEG data in the spectral modeling is much less than that of RGS data. We nevertheless found it beneficial to include the *Chandra* data into analysis, because due to the malfunctioning RGS2 CCD array #4, there are no RGS2 first-order data in the wavelength band between $\approx 20 - 24$ Å. This band covers the redshifted wavelengths of the O viii Lyα line for $z \approx 0.06 - 0.27$ and O vii Heα for $z \lesssim 0.11$ (which are the lines most likely to be detected), and because the second-order spectra of the RGS instruments have zero effective area at $\lambda \gtrsim 19$ Å, only LETG and MEG data can provide additional information to RGS1 first-order at these wavelengths. Also, since we are examining very weak spectral signatures, examining all the available data sets is useful for identifying false positives that could occur in individual data sets due to systematic effects such as calibration errors.

3. Data processing

3.1. XMM-Newton RGS

The RGS data were processed with the XMM-*Newton* SAS 16.0.0 software using the calibration file release XMM-CCF-REL-347. Both first- and second-order data were reduced with the rgsproc pipeline. We used somewhat more accurate processing options compared to the rgsproc defaults, in order to maximize the data quality for the examination of very weak spectral signals. Namely, we rejected the cool pixels from the data, and corrected for pixel-dependent energy offsets (rgsproc rgsenergy option withdiagoffset=yes). In addition, we decreased the aspect drift based frame grouping by a factor of two (i.e., driftbinsize=0.5″) and calculated the grating line spread functions using the full convolution space. It was confirmed that utilization of such more precise data processing options does improve the overall quality of the co-added spectra.

In addition, we created good time interval files by setting a threshold for the upper limit for the source flux, and filtered the data accordingly to remove the exposure time intervals contaminated by incidental Solar flares. We also employed the *rgsproc* binning algorithm to bin the data into 20 mÅ wavelength bins (i.e., twice the default bin width), a scheme that oversamples the instrument energy resolution by a factor of ≈ 3. The data was already rebinned during the spectral extraction phase because it provides numerically more stable results compared to rebinning the data later from the full resolution spectra, which was desirable since we aimed to use combined data sets to analyze signals close to the limits of detectability.

Table 1. List of FUV Absorbers Towards the 3C 273

z	Line ID	λ_{rest} (Å)	W (mÅ)	b (km s^{-1})	N log(cm^{-2})
0.0034	O vi	1031.9	26.6±4.1	~28.0	13.353 ± 0.077
0.0073	Lyα	1215.7	28.0±7.0	45.0±14.0	12.740 ± 0.110
0.0076	Lyα	1215.7	43.0±5.0	60.0±10.0	12.940 ± 0.065
0.0076	O vi	1031.9	14.0±4.0	25.0±9.0	13.110 ± 0.160
0.0876	Lyα	1215.7	55.0±1.0	42.0±2.0	13.050 ± 0.020
0.0898	Lyα	1215.7	86.0±4.0	46.0±2.0	13.220 ± 0.070
0.09017	O vi	1031.9	16.0±3.2	22.2±10.8	13.263 ± 0.110
0.09017	O vi	1037.6	14.1±5.0	22.2±10.8	13.263 ± 0.110
0.12005	O vi	1031.9	25.3±3.0	10.0±3.1	13.437 ± 0.058
0.12005	O vi	1037.6	17.8±2.9	10.0±3.1	13.437 ± 0.058

Notes. FUV redshifts of significantly detected BLA's ($b > 40$ km s^{-1}) and O vi absorbers in the 3C 273 sight-line (Tilton et al. 2012). The rest-frame line equivalent widths, W, line broadening parameters, b, and HI/O vi column densities, N, are listed with 1σ uncertainties (if available). The emphasized redshifts were considered in this work.

Table 2. Observational Sample

XMM-*Newton* RGS			*Chandra* HETG		*Chandra* LETG		
	Clean time (ks)			Clean time (ks)		Clean time (ks)	
OID	RGS1	RGS2	OID	ACIS	OID	ACIS	HRC
0126700301	61.7	59.8	14455	29.6	460		39.9
0126700601	25.9	25.1	17393	29.5	1198	38.2	
0126700701	15.9	15.5	18421	29.6	2464	29.5	29.7
0126700801	41.5	40.3	19867	26.9	2471	24.9	
0136550101	84.0	81.6	20709	29.6	3574	27.3	
0136550801	50.2	50.2	2463	26.7	4431	26.4	
0136551001	27.9	27.9	3456	24.5	5170	28.4	
0137551001	20.5	19.9	3457	24.9			
0159960101	57.9	57.9	3573	29.7			
0414190101	60.5	60.5	4430	27.2			
0414190301	30.0	30.3	459	38.7			
0414190401	31.0	30.8	5169	29.7			
0414190501	37.1	37.1	8375	29.6			
0414190701	36.0	36.0	9703	29.7			
0414190801	40.7	40.6					
0414191001	38.6	38.6					
0414191101	71.1	71.1					
0414191301	64.4	64.4					
0414191401	74.5	74.6					
Co-added Spectra:	730	723		405		174	69

Notes. Total clean times of the individual and co-added spectra. The co-added spectra were used in the analysis. In the case of RGS, two co-added spectra were generated for both instruments, one for each spectral order (first- and second-orders).

After reducing the RGS data sample as described above, we produced co-added spectra separately for each RGS instrument and spectral order using the `rgscombine` procedure. These co-added spectra were then converted into the SPEX[1] format with the `trafo` (v. 1.03) software. The `trafo` was used to create separate spectra for each co-added dataset, and in addition, to prepare a combined spectral file in which each of these co-added spectra were included (including the *Chandra* spectra as described in the following section). Using this combined spectral file allows us to flexibly and correctly fit the data from the different instruments simultaneously with SPEX (Sects. 4.3 and 5). This approach maximizes the data contributing to the analysis.

3.2. Chandra *instruments*

3.3. LETG

The *Chandra* LETG ACIS and HRC data were processed with CIAO v. 4.10 using the CALDB 4.7.9 calibration files. The data reduction was conducted using the `chandra_repro` script with the default parameter settings, and afterwards, the spectra of each of the instruments were co-added separately using the `combine_grating_spectra` spectral stacking tool. Both positive and negative order dispersion data were co-added when producing the ACIS and HRC spectral files for the analysis.

The statistical errors in all of the processed *Chandra* LETG observations used the Gehrels approximation for Poisson confidence intervals (as defined in Gehrels 1986), which are not

---

[1] http://www.sron.nl/SPEX

supported by the SPEX rebinning algorithm. Since the processed LETG data were over-sampled in the initial reduction, before converting the generated FITS data files into the SPEX format, we replaced the spectral data uncertainties with $\sqrt{N}$, where the N denotes the number of counts per spectral bin. The number N is in the range between $20-60$ cts/bin (HRC) and $30-150$ cts/bin (ACIS) in the studied wavelength band, meaning that the uncertainties are well approximated by $\sqrt{N}$ (as is shown, e.g., in Bonamente 2017).

Rebinning of the data was conducted using the ftools grppha software tool with a binning factor of two, resulting in a 30 mÅ bin size, or $0.6 \times \Delta\lambda$ channel width (we note that grppha rebinning is carried out by means of flagging, and is not a workaround for the rebinning issue mentioned above). Like with the RGS data, we then used trafo to create the separate co-added SPEX spectral files for each LETG instrument, and to add these spectra into the combined spectral file used in the simultaneous spectral modeling.

3.4. HETG

The HETG observations were reduced using the chandra_repro default processing, and the first-order data of the *Chandra* HETG Medium Energy Grating (MEG) arm were extracted. The data was co-added with the combine_grating_spectra tool and converted into the SPEX format with trafo. Like the data from the other instruments, we added this spectrum into the combined spectral file for the simultaneous analysis.

4. The analysis method

4.1. Data qualification

As described in Sect. 3, several steps were taken during data processing to minimize the risk of forming artificial absorption-like spectral features in the co-added spectra (especially in the case of the RGSs, which have the largest statistical weight in the sample). In addition, we applied two criteria throughout the analysis to further exclude sources of confusion. First, the closest CCD gap must be at least one HWHM away from the examined line centroid wavelength (only relevant to RGS since we co-added *Chandra* positive and negative orders), and second, no bad pixels or columns may be present in the immediate vicinity of examined lines (or more precisely, within the FWHM of the fitted line profile).

These criteria are important because small variations in telescope pointing (with respect to the dispersion direction) between different observations cause small shifts of the spectral wavelength scale at the detector plane. When such observations are co-added, the location of bad pixels and columns may vary in the detector wavelength space, which for a time-varying source such as 3C 273 can lead to an incorrectly defined effective area around the corresponding wavelength bins (more details of the issue can be found in Kaastra et al. 2011). As a result, spectral artifacts characteristically resembling those of absorption/emission lines may emerge in co-added spectra, or, if overlapping with an existing spectral feature, bias the measurements.

Manual inspection of RGS2 event files revealed bad pixels coinciding with the wavelength of the $z = 0.09017$ Ne ɪx Heα line in the RGS2 first-order data, and the data were therefore omitted from the analysis of this line. Other than that, no exclusion of data followed from these criteria for the line candidates examined in this study.

4.2. Redshift selection

To find the most likely locations of hot WHIM absorbers in the 3C 273 sight-line, we examined the FUV absorber data of the Tilton et al. (2012) FUSE+STIS survey (the sight-line has also recently been studied by Williger et al. 2010, Danforth & Shull 2008, Tripp et al. 2008 and Sembach et al. 2001), looking for the redshifts meeting our predetermined criteria. Namely, we were interested in the redshifts where: 1) at least two statistically significant metal absorption lines have been measured in the FUV, indicating a high concentration of metals in the absorber (we note that significant detections of two lines, such as those of the O ɪv doublet, makes it very likely that the FUV redshift is correctly determined), or 2) a broad Lyman alpha line with $b > 70$ km s^{-1} has been measured, indicating that the gas temperature may be high enough to produce significant lines in the soft X-ray band (as $b = 70$ km s^{-1} corresponds to a $\approx 3 \times 10^5$ K gas temperature assuming pure thermal line broadening).

Criterion 2 was adopted because it could reveal high temperature absorbers where the O ɪv ion fraction is too low to enable significant detection of O ɪv lines in the FUV, although the numerical value for the b-limit was chosen simply to exclude number of uninteresting (low temperature) Lyα absorbers from the X-ray analysis. We note, however, that without further information on the processes contributing to the Lyα line widths (turbulence, spectral line blending, etc), the thermal information content of the line width measurements is limited (e.g., Tepper-Garcia et al. 2012).

Two redshifts met the former criterion (0.09017, 0.12005, see Table 1). The O ɪv line profiles at these redshifts were checked against spectral characteristics typically associated with high velocity outflows (e.g., line profile asymmetries, velocity-dependent partial coverings, time variability, line widths), to exclude the possibility that the absorption lines are related to a high velocity outflow from 3C 273. No such indications were found for any of the examined FUV lines, implying the line detections most likely relate to intergalactic absorbers. These two FUV redshifts were adopted for the X-ray follow up study.

4.3. Modelling the 3C 273 emission and Galactic absorption

The X-ray spectra used in this analysis are combinations of multiple exposures from different epochs of a time-varying source. In such co-added spectra, the physical information carried by the continuum shape is largely averaged away. Indeed, we found that even when using limited wavelength bands, the complex shape of the quasar continuum was poorly fitted with power-law models. We therefore chose to model the emission continua of each dataset independently with a non-physical 'spline' model, which is a model specifically designed for accurate modeling of X-ray continuum shapes in cases where the physics underlying the continuum shape is not sufficiently well known. Adopting a non-physical continuum model is also useful because it can compensate for possible wider band systematics in instrument effective area models, thus improving the accuracy of the examination of weak (and narrow) absorption features in the spectra, such as those expected for the hot WHIM absorbers.

In the analysis we used a 'spline' model that consists of 17 uniformly spaced grid points between 13 and 29 Å, thus providing 1 Å intervals for the grid points; This scheme was found to enable accurate modeling of the continua, while the grid being sparse enough not to model any line features in the spectra. We allowed the 'spline' y-parameters (i.e., the intensity) to vary throughout our analysis, so to ensure that the uncertainties in

Table 3. Foreground Galactic Absorption Model

Parameter	Galactic Neutral	Galactic Hot
$N_{\rm H}$ (10^{19} cm^{-2})	17.7 [†]	$4.8^{+0.6}_{-0.5}$
kT (keV)	5×10^{-4} [†]	0.127 ± 0.007
O	0.8 ± 0.1	1 [†]

Notes. Fitted (and fixed) values defining the foreground Galactic absorption model used throughout the X-ray analysis. The O abundances are given in Solar units relative to H. All other elements were fixed to the Solar values.
[†]Parameter was fixed during the minimization, see text for details.

the continuum modeling were always properly propagated into the uncertainties of the model parameters of interest. The fitting band was fixed to $14 - 28$ Å, which covers the most important transition lines of Ne ix, O vii-viii, and N vii for both considered FUV redshifts.

We built a Galactic absorption model consisting of a component for the neutral disk and another one for the hot halo. For the neutral gas, we used the SPEX CIE absorption model called 'hot' with the temperature fixed to 5×10^{-4} keV (SPEX 'neutral plasma model'), and the hydrogen column to $N_{\rm H} = 1.77 \times 10^{20}$ cm^{-2} [2]. Although the used hydrogen column density value has a 16 % systematic uncertainty (see Willingale et al. 2013), we found no benefit in letting it vary during the fits, because the 'spline' model is able to compensate for the possible bias in $N_{\rm H}$. Instead, we found that when using the SPEX default for the line-broadening parameter ($\sigma_v = b/\sqrt{2} = 100$ km s^{-1}), the Solar abundances highly overestimate the O i lines of the component (blend at 23.5 Å), which is a possible indication of O i line saturation. We therefore measure the O i column density by letting the model oxygen abundance vary, while adopting the line-of-sight Doppler spread parameter $b = 18.6$ km s^{-1} for the line widths, which has been found to describe the low ionization state Galactic lines towards the 3C 273 elsewhere (Savage et al. 1993). We point out that even if the X-ray instruments are insensitive to line width information of narrow features ($b <$ several hundred km s^{-1}), the $N_{\rm OI}$ will be correctly constrained by the equivalent width measurement over the doublet when the value of $b_{\rm OI}$ is known. This fit yielded log $N_{\rm OI}$(cm^{-2}) = $16.91^{+0.06}_{-0.09}$ (corresponding 0.8 times the Solar O abundance), a result in line with $N_{\rm OI}$ at other lines of sight with similar $N_{\rm H}$ (e.g., Cartledge et al. 2004). As far as we know, this is the most accurately constrained Galactic $N_{\rm OI}$ measurement towards 3C 273.

To model the Galactic hot halo absorption (see e.g., Fang et al. 2003), we prepared another SPEX 'hot' component where the free parameters were the electron temperature and $N_{\rm H}$, and the elemental abundances were fixed to Solar. Fits with a hot halo component alongside the neutral gas absorber yielded $kT = 0.127 \pm 0.007$ keV and $N_{\rm H} = 4.8^{+0.6}_{-0.5} \times 10^{19}$ cm^{-2} (Table 3).

The emission model with Galactic absorption, as described above, was used in all of the analysis described in the following sections. It is important to note that none of the freely varying parameters (as described above) were fixed at any point of the spectral analysis, to ensure proper error propagation in the calculation of the redshifted absorption component fit parameters. All the analyses were performed using SPEX version 3.03.00 with proto-Solar abundances of Lodders et al. (2009), which is the SPEX default, and the models were fitted using Cash Statistics (Cash 1979).

5. X-ray analysis and Results

To verify the wavelength-scale accuracy of the co-added spectra, we first checked each of the spectra against linear shifts. This was done using the strongest spectral feature present in the 3C 273 X-ray spectrum, the Galactic O vii Heα line at $\lambda = 21.602$ Å. We fitted the data around this feature with a model combining a Gaussian absorption line with the 'spline' continuum model, while letting the Gaussian line centroid wavelength and the line normalization parameter vary. We found that the centroid wavelengths of the Gaussian modeling were consistent with the rest wavelength of O vii Heα within the statistical uncertainties of $\lesssim 10$ mÅ (see Table 4). This was true for each instrument, and indicates a redshift accuracy of $\sigma_z \approx 0.0005$ (corresponding to velocity accuracy $\Delta v \approx 137$ km s^{-1} at $z = 0.09$, and ≈ 132 km s^{-1} at $z = 0.12$). We will utilize this accuracy further when comparing the redshifts of the X-ray lines with those of the FUV lines (Section 5.1.1), and with those of the large scale filaments (Section 6.1.1).

Two different models were investigated in the spectral analysis. These were the emission model with Galactic absorption (Sect. 4.3) combined with: 1) a redshifted 'slab' line absorption component (Model 1, Sect. 5.1), and 2) a redshifted gas absorption component in collisional ionization equilibrium with solar relative abundances, (Model 2, Sect. 5.2).

In addition to these models, we used a model combining Gaussian lines and the Galactic absorption model whenever determining absorption line centroid wavelengths in the spectra: This approach was used to avoid shifting of the 'spline' emission component energy grid, which would take place if letting the model redshift to vary during the fits.

The initial search for redshifted absorption lines was conducted by fitting Model 1 independently to the co-added spectra of different instruments and spectral orders, and then by fitting the co-added spectra simultaneously with the same model. Considering all these measurement results together, we searched for inconsistencies between the results given by different instruments, and if such were found, the hypothesis of an astrophysical line origin was rejected.

Model 1 was also used in examining the effects of systematics on the measurement results of the putative redshifted lines. Namely, we re-fitted the RGS1 first-order data, which has the largest statistical weight in our sample, after adding a 2% Poissonian noise component to the data (corresponding to the systematic calibration uncertainty level of RGS first-order data, see de Vries et al. 2015). We found this noise component to have negligible effect on the fit parameters of interest, and therefore omitted its use in the further analysis.

After mapping the redshifted line candidates, the main analysis of this work was conducted using the simultaneous fitting method with Model 2, ensuring that all the information in each of the co-added spectra was taken into account in the analysis. The simultaneous fitting of data from different instruments and spectral orders was conducted with the appropriate SPEX tools[3]. Technically, in these fits, all the absorption components were coupled (i.e., both Galactic and redshifted components) between the models of the different co-added spectra, while the 'spline' continuum emission models were uncoupled. With this method, the continua of all the separate datasets, observed at different epochs with different instruments, were fitted at a level which enabled the investigation of weak absorption components at high

---

[2] http://www.swift.ac.uk/analysis/nhtot/index.php

[3] http://var.sron.nl/SPEX-doc/manualv3.03.00.pdf

Table 4. X-ray Line Wavelengths

Line	Instrument				PREDICTED
	RGS1	ACIS (LETG)	HRC	ACIS (HETG)	
Galactic O VII	21.604 ± 0.004	21.599 ± 0.005	21.609 ± 0.014	21.611 ± 0.002	21.602
Ne IX ($z = 0.09$)	14.67 ± 0.02	14.66 ± 0.01	$14.70^{+0.07}_{-0.10}$	$14.67^{+0.01}_{-0.007}$	14.66
O VIII ($z = 0.09$)	$20.66^{+0.03}_{-0.02}$	20.66 ± 0.03	$20.69^{+0.03}_{-0.08}$	20.68^{1}	20.68

Notes. Measured line centroid wavelengths of the first-order co-added spectra. In the column PREDICTED the redshifted wavelenghts for $z = 0.09017$ are listed. All values are in Angstroms.
[1] Only the best-fit value is quoted due to the low S/N ratio.

accuracy (we get C-statistics/d.o.f.< 1.07 in the used $14 - 28$ Å fitting band).

5.1. The redshifted absorption line model (Model 1)

To search for X-ray absorption lines in the data, we added a redshifted SPEX 'slab' component to the absorbed emission model described in Sect. 4.3. The 'slab' component models the transmission of photons through an optically thin layer of gas, and enables measurement of column densities of different ion species while setting no constraints on the gas ionization balance. The 'slab' component does, however, include the relative intensities of the spectrum of transition lines produced by the examined ion, thus providing more accurate results as compared to modeling the data with a single line profile. The SPEX 'slab' absorption model fits the lines with the Voigt profile, in which the Gaussian component has an adjustable line broadening to account for the thermal and non-thermal velocity distributions of the absorbing gas. Because we did not have information on either of these components, and since the used instruments' energy resolution is insufficient to model the line shapes, we fixed the 'slab' line width parameter to the SPEX default value of 100 km s^{-1} at all times (corresponding $T \sim 10^7$ K thermal broadening for oxygen lines).

The spectral analysis was conducted by fitting the ion column densities of the 'slab' model's O VII-VIII, Ne IX, Fe XVII, and N VII ions one by one, while fixing all the other 'slab' ion columns to zero during each fit. Using this approach, we investigated both of the FUV guided redshifts (0.09017, 0.12005) by fixing the redshift to those values. We note that the major benefit of using the 'slab' model to search for possible absorption lines is that it can be used to obtain the ion columns without any knowledge of the gas temperature. Therefore the analysis with the 'slab' model set up useful limits for the examined ion column densities, whose credibility can be tested against the predictions of physically justified models, such as CIE.

5.1.1. Absorption line analysis results: z=0.09017

We began the line analysis at the O VI absorber redshift $z = 0.09017$. Because the hot WHIM absorption lines are expected to have equivalent widths of only $\lesssim 10$ mÅ (e.g., Oppenheimer et al. 2016; Wijers et al. 2019), the visual prominence of possible WHIM lines in the co-added spectra is expected to be weak. For this reason, any existing line features could easily be overlooked and interpreted as noise. However, if the absorption features do have an astrophysical origin, then one can improve their visual appearance by utilizing the procedure introduced in Kaastra et al. (2011). Following this method, the SAS program rgsfluxer was used to generate fluxed RGS1 and RGS2 spec-
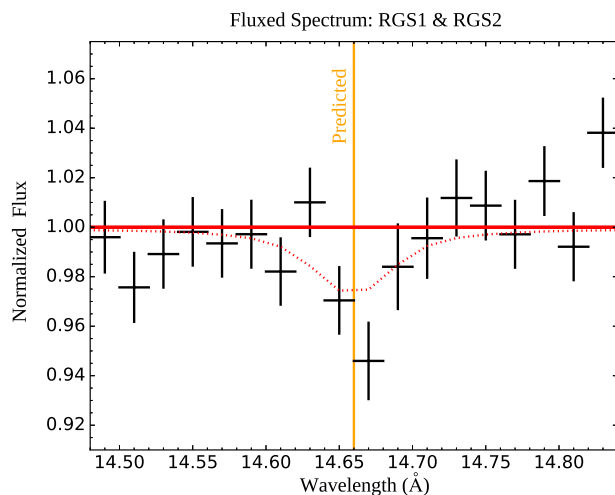

Fluxed Spectrum: RGS1 & RGS2

Fig. 1. Continuum normalized, co-added fluxed spectrum of RGS1 and RGS2 data at the wavelength around the putative redshift 0.09017 Ne IX Heα absorption line. The FUV predicted line centroid wavelength is shown with the orange line, while the dotted red curve shows the expected absorption signal based on the simultanous fitting of XMM-*Newton* and *Chandra* data with the redshifted *slab* model (Sect. 5.1.1).

tra for each spectral order, which were then combined using the SPEX tool rgsfluxcombine to generate a single fluxed spectrum. We note that producing a fluxed spectrum also works as an independent sanity check, because the tool is less prone to produce stacking artifacts than rgscombine. We found that the resulting spectrum with increased photon statistics (at the wavelength bands where available) indeed shows a strengthened absorption feature at the wavelength ≈ 14.66 Å, which corresponds to the redshifted wavelength of the Ne IX Heα line at $z = 0.09017$ (Fig. 1).

Quantitative analysis of Ne IX by simultaneous fitting of Model 1 to the co-added XMM-*Newton* and *Chandra* data yielded $W = 2.7 \pm 0.9$ mÅ for the rest-frame equivalent width of the Ne IX Heα line, corresponding to an ion column density $\log N_{\text{Ne IX}}(\text{cm}^{-2}) = 15.4^{+0.1}_{-0.2}$ for Ne IX. In Fig. 1 we plot this predicted absorption signal for the Ne IX Heα line on top of the fluxed spectrum for comparison. In addition, we found an absorption line feature at the wavelength corresponding the $z = 0.09017$ O VIII Lyα line, for which we measured a rest-frame $W = 4.3 \pm 1.6$ mÅ corresponding $\log N_{\text{OVIII}}(\text{cm}^{-2}) = 15.5 \pm 0.2$. In case of O VIII Ly$\alpha$, the application of the fluxed spectrum method was not useful, because the corresponding wavelength band is only observable in the RGS first-order spectrum and accordingly no improvement of photon statistics was available. We

point out that the O vii Heα line, which is typically expected to be the strongest X-ray WHIM line, would blend with the (strong) Galactic O i line ($\lambda_{z=0}^{O\,I} \approx 23.51$ Å, $\lambda_{z=0.09017}^{O\,VII} \approx 23.55$ Å), thus preventing the analysis of this line. Accordingly, we are only able to report here the weak upper limits for O vii at $z = 0.09017$ based on the fits to the non-blended transition lines, including the O vii Heβ and others.

To double-check the measurement results obtained from simultaneous fitting with Model 1 (see the best-fit model on top of each of the individual co-added spectra in Figs. 3 and 4), we analyzed each of the co-added spectra separately with the same model. Similarly to the simultaneous modeling, the separate fits yielded ion column densities of the order of 10^{15} cm^{-2} for both ions (Ne ix, O viii) in each co-added dataset, and no inconsistencies were found between different instruments. We present the complete line analysis results, including both the simultaneous and the individual fits to the co-added spectra, in the uppermost panels of Table 5.

The co-added spectra were also studied independently by adopting a model combining the absorbed emission model (Sect. 4.3) with Gaussian absorption lines, to confirm that the spectral features suspected as redshifted Ne ix and O viii lines were indeed centered at the wavelengths predicted by the FUV redshift. The Gaussian line model was adopted for this analysis because of the technical limitations of 'slab' modeling in this context, as mentioned in Sect. 5. In the fits we set the line parameters according to the results discussed above, and re-fitted the data while allowing the Gaussian line centroid wavelengths and line normalization parameters to vary. We found that within the error margins, the Gaussian lines yielded centroid wavelengths consistent with those predicted by the FUV redshift, and that this was true for both examined lines for each available instrument (see Table 4). Since the wavelength-scale of the X-ray data was found to be accurate to $\sigma_z \approx 0.0005$, or $\Delta v_{X-ray} \approx 137$ km s^{-1} (Section 5), and as the FUV redshifts are only expected to have a z uncertainty of $\Delta z_{FUV} \sim 3 \times 10^{-5}$ ($\Delta v_{FUV} \approx 8$ km s^{-1}), the hypothesis of spatial co-location of the FUV and X-ray absorbers was found to be supported by all the observational data.

Finally, since it is possible that spectral co-addition produces small artifacts which can be erroneously interpreted as astrophysical lines, and because the two tentative X-ray lines only have equivalent widths of few mÅ, we chose to investigate this issue further. Here we used the RGS1 first-order data, which contains the majority of the statistical weight in the simultaneous fits and is co-added from 19 different observations. We refitted the RGS1 first-order data using the original, non-stacked spectra and applied the same method used in the simultaneous fits to the spectra of different instruments and spectral orders (i.e., coupled absorption - uncoupled emission). The results obtained for both absorption lines were practically identical to the fits to the co-added RGS1 data (Table 6), thus confirming that the examined spectral features are not co-adding artifacts.

To conclude the results of the line analysis, Model 1 yielded $N_{ion} \sim 10^{15}$ cm^{-2} ion column densities for O viii and Ne ix, which are in the range expected for hot WHIM absorbers. We found that all the instruments agree with these results, and that the features appear in the spectra at the wavelengths predicted by the FUV absorber redshift. The O viii and Ne ix ion fractions peak at coinciding temperature ranges (i.e., $T \approx 10^{6-6.5}$ K), and hence the two ions are likely indicators of a common gas phase for which the 'slab' modeling yields a 3.9σ (quadratically summed) detection level. We therefore adopted the Ne ix and O viii lines as hot WHIM line candidates at the O vi absorber
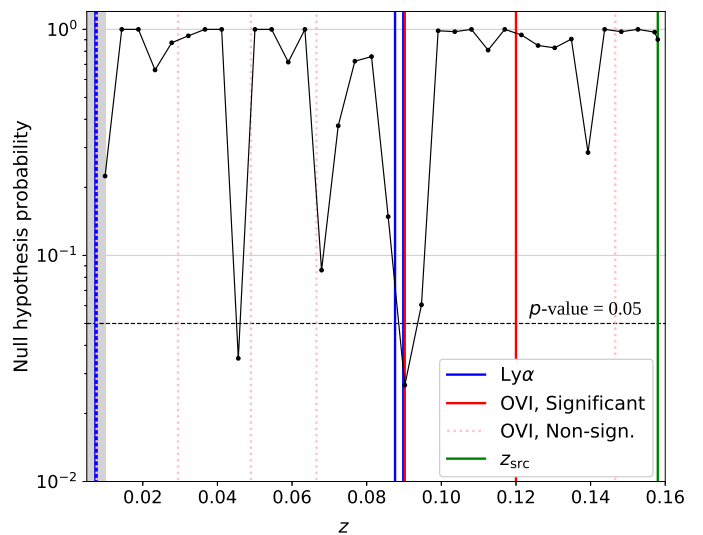

Fig. 2. Statistical probability of the Null hypothesis validity over the redshift range $0.005 - 0.158$. The Null hypothesis is the emission model with Galactic absorption, which is compared to the WHIM hypothesis, i.e., a model including a redshifted hot ($T = 10^{6-7}$ K) CIE absorption component. The dashed black line marks the commonly adopted Null hypothesis rejection limit, $p = 0.05$. The FUV redshifts listed in Table 1 are shown together with the non-significant O vi doublet detections (from Table 4 in Tilton et al. 2012). The shaded color marks the confusion region of the redshifted absorption component with the Galactic hot halo.

redshift $z = 0.09017$. The obtained measurement results regarding these line candidates are next compared to the constraints from the physical WHIM absorption model (Model 2) in Sect. 5.2.

5.1.2. Absorption line analysis results: z=0.12005

The 'slab' analysis for the FUV redshift $z = 0.12005$ revealed no hot absorption line candidates at the predicted centroid wavelengths of any of the lines of interest (as listed in Sect. 5.1), making it uninteresting for the further spectral analysis. The X-ray non-detection is concordant with the earlier results of Tripp et al. (2008), where it was found that the O vi, HI Lyα line widths yield $T < 10^{4.7}$ K (3σ upper limit) for the FUV detected gas at the 3C 273 $z = 0.12$ absorber. These X-ray and FUV results may indicate that this absorber only has a warm component.

Furthermore, we note that the non-detection of hot phase ions at $z = 0.12$ means, for instance, that the 1σ limit on the O vi absorber associated N_{OVIII} reduces from $\log N_{OVIII}(\text{cm}^{-2}) = 15.7$ (as measured at $z = 0.09$) to 15.1 when both of the O vi absorber redshifts are considered simultaneously. This limit agrees well with the earlier results of Yao et al. (2009), where they measured a $\log N_{OVIII}(\text{cm}^{-2}) = 15.63$ 95 % upper limit on O viii columns associated with the strong O vi WHIM absorbers. This upper limit comes from an analysis of z_{OVI} blueshifted, stacked X-ray spectra from 6 different sight-lines (refer to Yao et al. 2009 for details). We note however, that while the z_{OVI} based stacking of the X-ray data increases the spectral S/N -ratio, the sensitivity to measure the hot phase ion signals may be compromised in this method. This is because X-ray band detectable ion columns are produced in more limited WHIM parameter space region than FUV detectable O vi columns, and hence frequent non-detections of hot ion species are expected, which can effec-

tively hide the X-ray signals in the z_{OVI} shifted, stacked spectra. We will investigate the co-occurrence rate of detectable O vi and O viii ion columns in the WHIM absorbers in more detail in Sect. 7.

5.2. Collisional ionization equilibrium modeling (Model 2)

The analysis with the 'slab' absorption model (Sects. 5.1.1 and 5.1.2) yielded two absorption line candidates at the wavelengths matching those of Ne ix and O viii lines at the FUV absorber redshift $z = 0.09017$ (Table 4). The ionization temperatures of Ne ix and O viii are similar, and indicate $\log(T(K)) > 6$ for the absorbing gas. Since at these temperatures photo-ionization is expected to be less important and collisional ionization equilibrium (CIE) is likely, we tested this hypothesis and modeled the data by adding a redshifted CIE absorption component with solar relative abundances to the emission model with Galactic absorption (hereafter CIE WHIM). The CIE WHIM modeling was performed using the simultaneous fitting of the co-added spectra, except that of the RGS2 first-order, which was omitted from the analysis due to the absence of reliable data at the wavelengths of either of the two putative absorption lines.

To ensure that the CIE WHIM model robustly detects the weak signals of interest, we utilized the model in a blind search test over the redshift range $z = 0.005 - 0.1578$. In this test, the lower z limit was chosen large enough to avoid considerable blending with the absorption lines of the hot Galactic halo, while the upper z limit corresponds to the nominal redshift of 3C 273. The redshift range was examined in steps so that each z-increment corresponded to a 60 mÅ wavelength shift of the Ne ix line centroid in the spectra. At each step the co-added spectra were fitted with the CIE WHIM model, and the fit C-statistics compared to that obtained without the redshifted component included (Null hypothesis). The improvement of the fit statistics due to the addition of the redshifted absorption component were converted into a Null hypothesis probability using a modified F-test (modified, since we used C-statistics instead of χ^2 as a figure of merit). The results of this test are illustrated in Fig. 2. As might be expected based on the results of the 'slab' analysis, we found that the lowest p-value is indeed obtained at $z \approx 0.09$ ($p \approx 0.027$), while at $z \approx 0.12$ the Null hypothesis is valid. These findings support the applicability of the CIE WHIM modeling in the context of this study.

In addition to $z = 0.09$, the p-value falls below the often adopted Null hypothesis rejection limit, $p = 0.05$, at $z \approx 0.045$ ($p \approx 0.035$). This redshift does not fulfill our predetermined FUV z-criteria (Sect. 4.2), but we will make a few remarks on this minimum here. The best-fit CIE model is described by $kT \approx 0.10$ keV ($\approx 1.1 \times 10^6$ K) and $N_H \approx 4.6 \times 10^{18}$ cm^{-2}, which together define a model producing one detectable absorption line in the examined spectral band (O vii Heα, EW≈ 5 mÅ). Inspection of the spectra reveals that this model is minimized to a line-like feature present in the RGS1 first-order data at $\lambda = 22.55$ Å, while the other instruments' data lack the sensitivity to confirm the existence of this feature. We note that the best-fit model does not predict any detectable signal in the FUV band (e.g., $\log N_{OVI}(\text{cm}^{-2}) < 13$) and that there are no FUV detections at the corresponding redshift. In the absence of such supporting information, and since the best-fit CIE model is effectively a single line model, it remains uncertain whether the fit reveals CIE state O vii absorption at $z \approx 0.045$, or some other (non-CIE) ionic line at a different redshift. Lacking additional observational evidence to support the physical origin of this feature, or to verify that the

suspected redshift is correct, we will not consider the possible $z \approx 0.045$ signal further in this work.

5.2.1. CIE absorber analysis results: z=0.09017

The analysis results of the CIE WHIM modeling at the FUV redshift $z = 0.09017$ are listed in the bottom panel of Table 5. The CIE model yielded a gas temperature $kT = 0.26 \pm 0.03$ keV ($\log T(\text{K}) = 6.48 \pm 0.05$) and hydrogen column density $N_H = 1.3^{+0.6}_{-0.5} \times 10^{19}$ cm^{-2} (when $Z = Z_\odot$), corresponding ion column densities $\log N_{\text{NeIX}}$ (cm^{-2}) $= 14.9 \pm 0.2$ and $\log N_{\text{OVIII}}$ (cm^{-2}) $= 15.4 \pm 0.2$. We note that no other lines with comparable equivalent widths were predicted in the fitting band, nor in the wavelength range accessible to any of the used instruments (i.e., $\lambda \approx 3 - 175$ Å). We find that while the 'slab' and CIE modeling yield matching ion columns for O viii ($\log N^{slab}_{\text{OVIII}}(\text{cm}^{-2}) = 15.5 \pm 0.2$, $\log N^{\text{CIE}}_{\text{OVIII}}(\text{cm}^{-2}) = 15.4 \pm 0.2$), the CIE-predicted Ne ix column is lower than obtained with 'slab' modeling ($\log N^{slab}_{\text{NeIX}} = 15.4^{+0.1}_{-0.2}$, $\log N^{\text{CIE}}_{\text{NeIX}} = 14.9 \pm 0.2$). Such discrepancy could be explained, for instance, by Ne ix excess within the particular integration path through the absorber, or as an indication of small deviations from the ionization equilibrium at the absorbing gas. We will consider this discrepancy further in Sect. 7.

We also find that the CIE WHIM model predicted O vi column density, $\log N^{\text{CIE}}_{\text{OVI}}(\text{cm}^{-2}) = 12.2 \pm 0.2$, is an order of a magnitude lower than indicated by the FUV data, $\log N^{\text{FUV}}_{\text{OVI}}(\text{cm}^{-2}) = 13.263 \pm 0.110$. The measured O vi absorption cannot therefore be explained by hot, collisionally ionized gas. The same conclusion can also be drawn from the FUV measured O vi line broadening (Table 1), which is smaller than thermal broadening at CIE WHIM model temperatures. We will examine these discrepancies in detail in Sects. 6.3 and 7.

The temperature of the CIE WHIM model is remarkably tightly constrained. This can be understood through the constraints set by both the detections and non-detections of the most important absorption lines in the temperature range in question (see Fig. 5). Namely, the line equivalent width (W) ratio between the Fe xvii resonance line and O viii Lyα is very sensitive to the temperature, and thus the non-detection of Fe xvii sets a strict upper limit on the temperature. At low temperature end, non-detections of O vii and N vii lines set constraints for the model temperature.

In Fig. 6, we show the best-fit CIE WHIM model prediction for the redshifted O vii Heα line, which could not be examined independently due to blending with the Galactic O i line but, nevertheless, contributes in constraining the free parameters of the CIE model. It is evident from this figure that within the obtained temperature constraints, the O vii Heα would not be strong enough for detection even without the incidental line blending.

6. Interpretation of the results

Here we discuss physical interpretations regarding to measurement results of X-ray and FUV absorption at $z = 0.09$, assuming that both FUV and X-ray detections are real. First, in Sect. 6.1.1, we consider the possibility that the absorbers are part of a WHIM filament crossing the sight-line at $z \approx 0.09$. In Sect. 6.2, we speculate about an alternative interpretation that the absorption signals come from the Circumgalactic medium (CGM) of individual galaxies with small impact parameters to the sight-line. Then in Sect. 6.3, we discuss the thermal structure of the absorbing gas in view of the observational results.
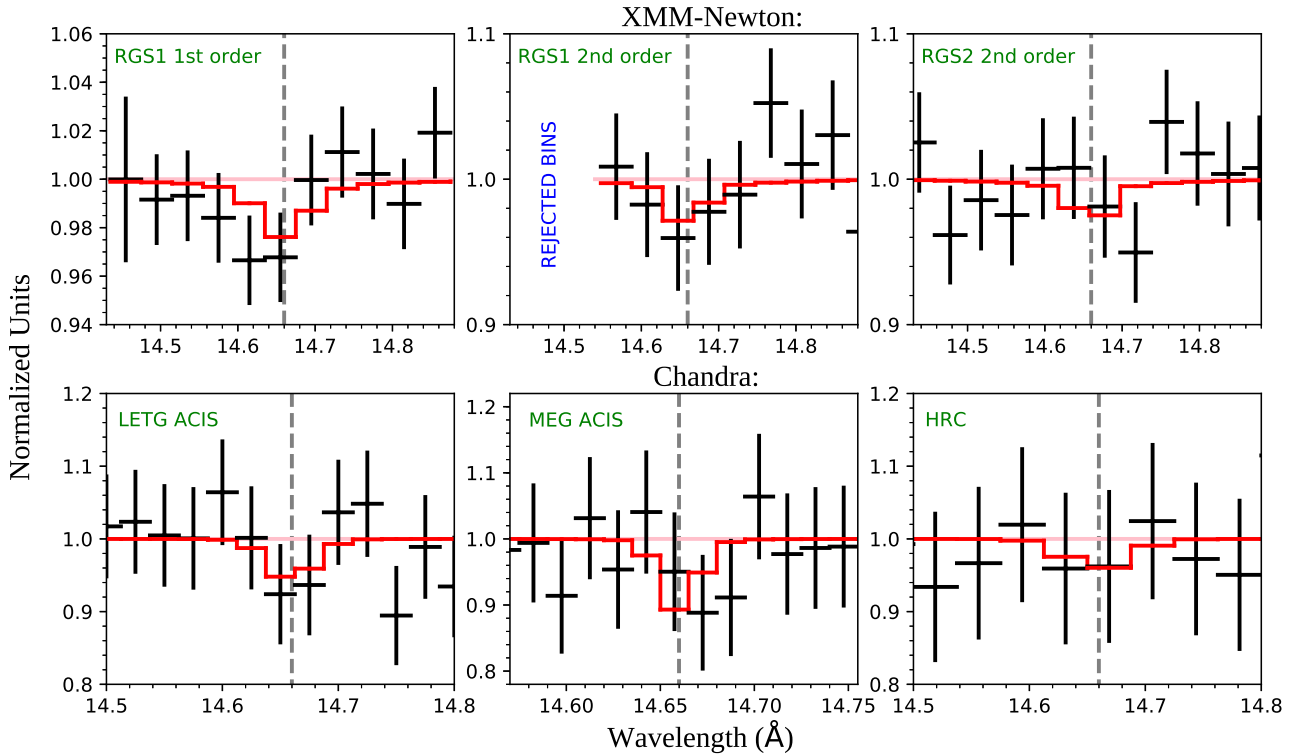
Fig. 3. Normalized data (crosses) and the best-fit model (red line) of the $z = 0.09017$ Ne ix line (the FUV predicted line centroid wavelength is marked with a dashed line) for all the instruments and spectral orders employed. The normalization is done by dividing the spectra by the best-fit continuum model. The best-fit model was simultaneously fitted to RGS1 (first and second dispersion orders), RGS2 (second-order), LETG ACIS (first-order), MEG ACIS (first-order) and HRC data, while the RGS2 first-order data was omitted due to a bad column near the centroid wavelength of the line. The missing bins in RGS1 second-order were rejected by the reduction software due to bad response. The spectral data was rebinned for this illustration to improve the S/N -ratio.
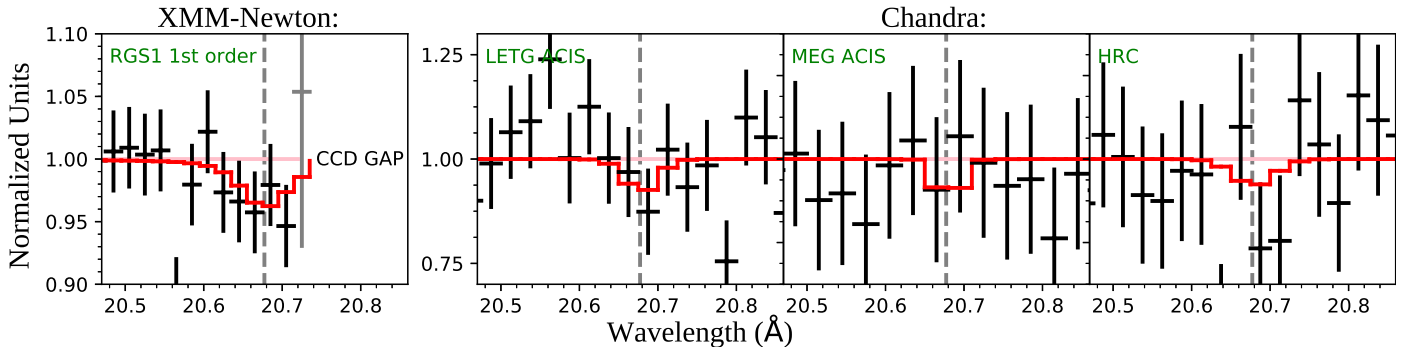

Fig. 4. As Fig. 3 but for O viii. The grey bin near the border of the RGS1 CCD gap was not used in the minimization, but demonstrates a type of spectral artifact that can be produced when observations from different epochs and slightly different pointings with respect to the dispersion direction are co-added.

6.1. Galactic environment

We studied the SDSS galaxy distribution in the 3C 273 sight-line around the FUV absorbers at $z \approx 0.09$. 3C 273 is located in the main SDSS survey region. Our galaxy distribution analysis is based on the SDSS flux-limited ($m_r < 17.77$) catalog. The catalogue and data preparation are described in Tempel et al. (2014b, 2017).

We employed the Bisous model in order to detect possible galactic filaments, which are expected to harbour a large fraction of the local baryons in the form of the WHIM. The Bisous model is a marked object point process that is specifically designed to detect galactic filaments in spectroscopic galaxy distribution data, as described in Tempel et al. (2014a, 2016). The scale of the extracted filaments in the SDSS data is ~1 Mpc, which corresponds to the scale of large-scale intergalactic medium filaments in simulations (based on visual inspection of simulated filaments in Kooistra et al. 2017, see also the discussion in Schaye 2001). Thus, if a filament axis passes the sight-line at a distance closer than 1 Mpc, we consider it to be crossing the sight-line.

6.1.1. Absorption by WHIM filaments at z=0.09

We detected two filaments of ~10 Mpc length at $z \approx 0.09$ around the 3C 273 sight-line, as presented in Fig. 7 (see also the discussions in Williger et al. 2010). Filament F1 passes the 3C 273 sight line at a 3D distance smaller than 0.5 Mpc, that is, closer

Table 5. Reshifted Absorber at $z = 0.09017$

Parameter	SIMULT. FIT	RGS1 1st	RGS1 2nd	RGS2 2nd	LETG ACIS	LETG HRC	MEG ACIS
				Ne IX			
$\log N_{\mathrm{NeIX}}(\mathrm{cm}^{-2})$	$15.4^{+0.1}_{-0.2}$	$15.5^{+0.2}_{-0.4}$	< 15.8	< 15.6	$15.6^{+0.2}_{-0.5}$	< 15.9	$15.3^{+0.25}_{-0.6}$
$W_{\mathrm{He}\alpha}$ (mÅ)	2.7 ± 0.9	3.4 ± 1.8	$2.6^{+2.9}_{-2.6}$	$0.9^{+2.8}_{-0.9}$	$4.1^{+2.5}_{-2.6}$	$2.0^{+5.0}_{-2.0}$	$2.4^{+1.6}_{-1.7}$
σ	2.9	1.8	-	-	1.4	-	1.4
c-stat/dof	3691/3451	642/557	266/220	231/197	548/539	546/539	1434/1379
				O VIII			
$\log N_{\mathrm{OVIII}}(\mathrm{cm}^{-2})$	15.5 ± 0.2	$15.5^{+0.2}_{-0.3}$	n/a	n/a	$15.6^{+0.3}_{-0.7}$	$15.9^{+0.3}_{-0.5}$	< 15.6
$W_{\mathrm{Ly}\alpha}$ (mÅ)	4.3 ± 1.6	$4.3^{+2.2}_{-2.1}$	n/a	n/a	$4.9^{+3.9}_{-3.8}$	$9.6^{+6.9}_{-6.6}$	$1.1^{+4.1}_{-1.1}$
σ	2.6	2.1	n/a	n/a	1.3	1.5	-
c-stat/dof	3178/3026	641/557	n/a	n/a	549/539	544/539	1436/1379
				O VII			
$\log N_{\mathrm{OVII}}(\mathrm{cm}^{-2})$	< 15.5 *						
$W_{\mathrm{He}\alpha}$ (mÅ)	< 8.6 *						
c-stat/dof	3146/2982						
				CIE			
kT (keV)	0.26 ± 0.03						
N_{H} ($Z_\odot/Z \times 10^{19}$ cm^{-2})	$1.3^{+0.6}_{-0.5}$						
$\log N_{\mathrm{Ne\,IX}}(\mathrm{cm}^{-2})$	14.9 ± 0.2						
$\log N_{\mathrm{O\,VIII}}(\mathrm{cm}^{-2})$	15.4 ± 0.2						
$\log N_{\mathrm{O\,VII}}(\mathrm{cm}^{-2})$	14.8 ± 0.2						
$\log N_{\mathrm{O\,VI}}(\mathrm{cm}^{-2})$	12.2 ± 0.2						
c-stat/dof	5156/4850						

Notes. Spectral modeling of the $z = 0.09017$ X-ray absorber. The results of the 'slab' modeling of Ne IX ($\lambda_0 = 13.447$ Å), O VIII (blend at $\lambda_0 \approx 18.97$ Å) and O VII ($\lambda_0 = 21.602$ Å) are shown in the three uppermost panels; The rest-frame line equivalent widths of the most important absorption lines are denoted by W, while the σ refers to the statistical detection significance level of the ion as yielded by the *slab* modeling. The first column reports the results obtained from a simultaneous fit to the individual, co-added data sets, whereas the last 6 columns list the results when these co-added data sets are modeled separately. 1σ upper limits for 'slab' column densities are quoted if the line was not detected in individual spectra. The $z = 0.09017$ CIE modeling results are listed in the bottom panel.
The n/a refers to zero effective area around the wavelengths of interest. The RGS2 first-order data was not included in the fits as it misses the data around the wavelengths of all the examined line features. All the quoted uncertainties correspond to 1σ confidence levels.
* Due to the spectral line blending with Galactic O I lines, the O VII upper limits were derived excluding the band of the O VII Heα line.

Table 6. Fits to Stacked and Non-stacked Data

Parameter	Individual	Co-added
W, Ne IX (mÅ)	3.3 ± 1.8	3.4 ± 1.8
$\log N_{\mathrm{Ne\,IX}}(\mathrm{cm}^{-2})$	$15.51^{+0.22}_{-0.37}$	$15.51^{+0.22}_{-0.37}$
σ	1.8	1.8
c-stat/dof	11270/10593	642/557
W, O VIII (mÅ)	$4.1^{+2.2}_{-2.1}$	$4.3^{+2.2}_{-2.1}$
$\log N_{\mathrm{O\,VIII}}(\mathrm{cm}^{-2})$	$15.51^{+0.20}_{-0.32}$	$15.54^{+0.19}_{-0.30}$
σ	1.9	2.1
c-stat/dof	11269/10593	641/557

Notes. Comparison between the results of simultaneous fits to the 19 individual RGS1 first-order spectra (column "Individual"), and the results obtained when fitting the co-added spectrum of the same data-set (column "Co-added"). The W denotes the rest-frame equivalent widths of the major transition line of the ion, while the σ marks the nominal detection significance levels for the fitted lines.

than the expected filament width. Thus we consider that 3C 273 sight line crosses the core of the filament F1 at a co-moving heliocentric distance of ≈ 378 Mpc. This crossing point is consistent with the FUV and X-ray line centroids, if their redshifts are entirely due to the Hubble expansion. Filament F2 (see Fig. 7) crosses the 3C 273 sight-line ~ 10 Mpc away from the FUV centroid (closer to the observer), if the FUV absorber has no significant radial peculiar velocity component. Assuming alternatively

that the FUV absorber is the filament F2, it should have a radial velocity of 800 km s^{-1}. Infall with such a high velocity is unlikely, indicating that the FUV absorber is located close to the crossing point of filament F1 and the sight-line towards 3C 273 (see Fig. 7). Given the relatively large statistical uncertainties in the redshift of the X-ray absorber, and allowing an infall velocity of a few 100 km s^{-1} (i.e., a shift of a few Mpc in location), we cannot determine whether F1 or F2 is a more likely location for the X-ray absorber. However, the consistency of the FUV and X-ray centroid redshifts with each other and with the location of the major galactic filament F1 suggests that both absorbers are due to WHIM in F1.

Using the galaxy distribution we also generated a three dimensional luminosity density (LD) field (for details, see Liivamagi et al. 2012; Tempel et al. 2014b). The LD profile along the sight-line (see Fig. 7) peaks at the crossing points of filaments F1 and F2. Assuming that the X-ray absorber is located at F1, and following the procedures described in Nevalainen et al. (2015), we converted the luminosity density profile along the sight-line in the radial range of 375–381 Mpc into a WHIM hydrogen column density estimate of $N_{\mathrm{H,F1}} \sim 2 \times 10^{19}$ cm^{-2}. (Currently we cannot explicitly account for the possible selection effect induced uncertainties in the total error budget of N_{H}, and consequently we only give the best estimate value here). The perpendicular orientation of F1 relative to the 3C 273 sight-line provides a minimal path length (~ 1 Mpc) through the filament and thus gives a relatively low column density. Assuming a 1
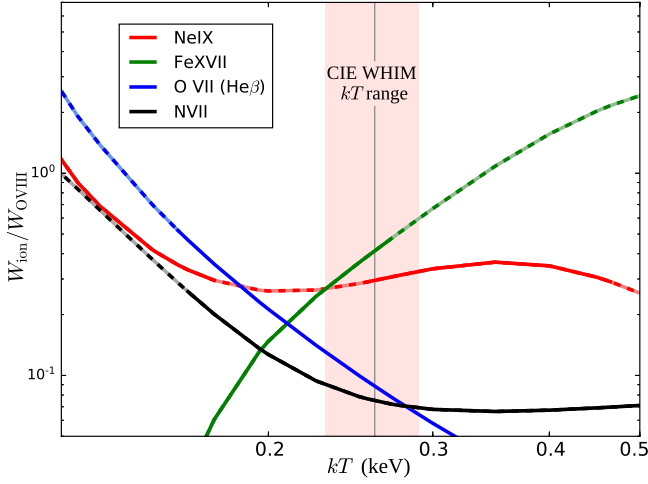
Fig. 5. Origin of temperature constraints in CIE WHIM modeling. The figure illustrates CIE model temperature dependencies of various ionic line strengths relative to that of the O VIII Lyman α line. The dashed sections mark the regions where the $W_{\text{ion}}/W_{\text{OVIII}}$ ratio is inconsistent with the 1σ limits of *slab* modeling. The ions shown in the figure produce the most important absorption lines in the spectra in the examined wavelength band of 14–28 Å and thus constrain the CIE temperature, marked with the shaded region. The data of the strongest available ionic lines were used to generate this figure.
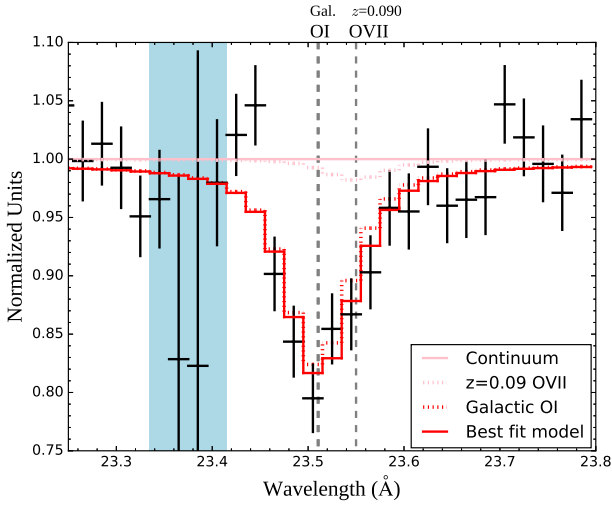
Fig. 6. Zoom-in on the continuum-normalized, RGS1 first-order co-added spectrum at the wavelength band of the Galactic O I ($\lambda \approx 23.51$ Å) doublet, where the best-fit CIE WHIM model predicts an O VII Heα line ($\lambda \approx 23.55$ Å). The different model components comprising the best-fit model (red line) are shown separately. The shaded area marks bins affected by instrumental absorption.

Mpc path length and a constant density along the path yields a WHIM hydrogen number density of $\sim 6 \times 10^{-6}$ cm^{-3}, that is, a baryon overdensity of ~ 20, a value consistent with the WHIM in simulations. We note that the estimate of the total hydrogen column density of F1 ($\sim 2 \times 10^{19}$ cm^{-2}) is consistent with the value the X-ray data yielded for N_{H} (Table 5), if the WHIM metallicity is $\sim 10^{-1}$ Solar (as we find that $N_{\text{H}}^{X-ray} \gg N_{\text{H}}^{FUV}$, see details in Sect. 6.3).
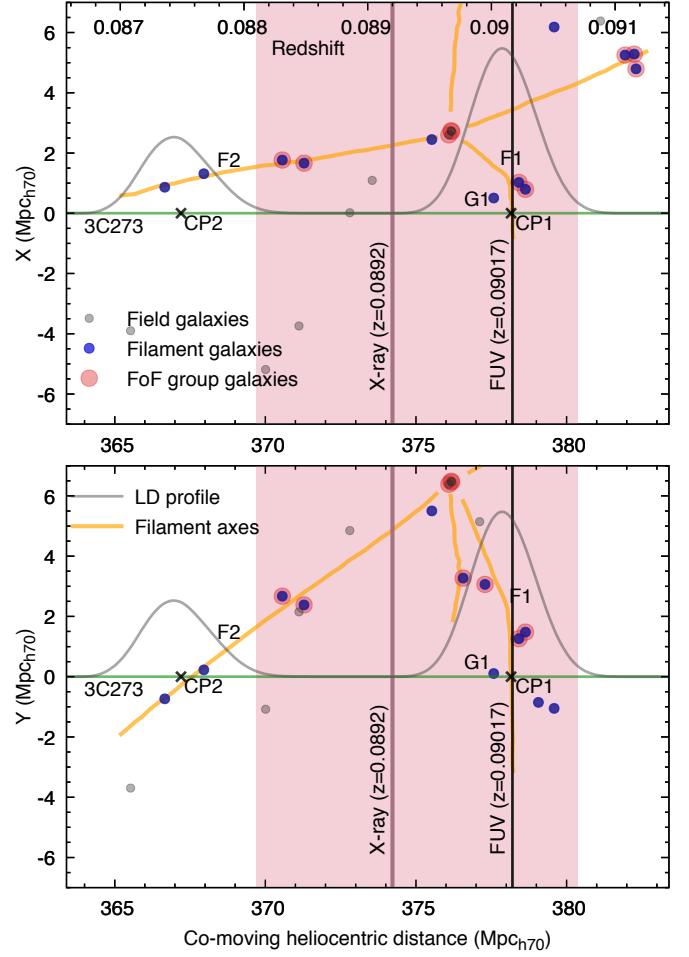

Fig. 7. Filament analysis for 3C 273 sight-line near $z = 0.09$. The figure shows the distribution of SDSS galaxies (points) in two orthogonal projections (upper and lower panels), each of which are 20 Mpc thick. Blue points represent galaxies in filaments and red points indicate additional galaxies in friends-of-friends groups. The detected filament axes F1 and F2, and the associated luminosity density profiles are denoted by yellow lines and grey curves, respectively. The crossing points of the filaments F1 and F2 and the sight-line to 3C 273 are denoted with labels "CP1" and "CP2", respectively. The redshift of the O VI absorption is marked with the black vertical line, whereas the pink vertical line and area correspond to the X-ray measured O VIII line centroid and its 1σ measurement uncertainty, obtained in the Gaussian model fit to the O VIII Lyα feature (see Table 4)

6.2. Absorption by Circumgalactic Medium at z=0.09

We next considered the possibility that the haloes of galaxies close to the 3C 273 sight-line are the the dominant source of the FUV and X-ray absorption we associated with the F1 filament above. The most likely object to provide sufficient ion columns is G1 (see Fig. 7), the nearest galaxy to the sight-line ($b_{\text{impact}} \approx 500$ kpc) at a redshift close to F1. It is a spiral galaxy with $M_r = -21.1$, and hence photo-metrically similar to the Milky Way (Licquia et al. 2015). Using the `IllustrisTNG` simulations (Nelson et al. 2018b) for galaxies with halo mass $\log(M_{\text{halo}}) = 12.0$, that is, the same as for the Milky Way, for $b_{\text{impact}} \approx 500$ kpc we obtained an average $\log N_{\text{OVI}}(\text{cm}^{-2}) \approx 12.2$ with 1σ halo-to-halo variation of $\approx 9.8 - 13.0$ (D. Nelson priv. comm.). Therefore the O VI column of the $z = 0.09$ absorber, $\log(N_{\text{OVI}}) = 13.263 \pm 0.110$ (Tilton et al. 2012), seems consis-
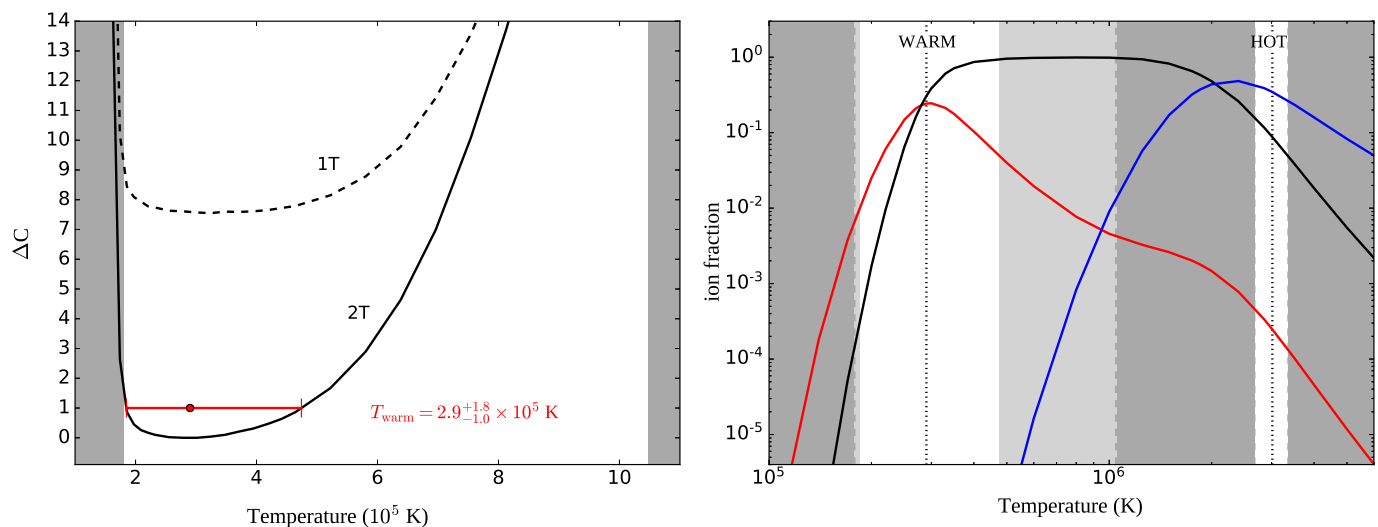
Fig. 8. Thermal properties of the absorbing gas at $z = 0.09017$ assuming CIE. Left: Temperature dependence of the two-phase absorption model fit statistics to the X-ray data (black solid curve) when N_{OVI} is fixed to the FUV measured value. The shaded areas mark the forbidden regions based on the FUV measurements (the lower limit is yielded by the limits on N_{CIII} and N_{OVI}, whereas the upper limit is set by the O VI line broadening). The 1T curve shows the X-ray model fit statistics without the hot absorption component included, and is plotted for reference. Right: O VI (red), O VII (black) and O VIII (blue) ion fractions over the T-ranges of the warm and hot CIE components. The dotted lines mark the best-fit temperatures for both phases, while the white regions mark the 1σ uncertainty limits as yielded by X-ray data. The light gray shaded regions show the improvement which X-ray data provides to the T_{warm} determination as compared to the limits obtained with FUV data.

tent with absorption through the halo of G1. However, given that the halo-to-halo variation spans over three order of magnitudes, the consistency may be only coincidental and one cannot determine the origin of the absorption without further information on the absorber properties.

When it comes to the hot phase, we do not have similar simulation results available, and the relevant observational information is also very limited. As it stands, hot ($\sim 10^6$ K) coronae around spiral galaxies have only been directly measured for a few nearby massive spirals, and even in these cases the photon statistics have limited the detailed analysis to the centermost halo regions. For instance, Bogdan et al. (2013) reported hot haloes around the NGC 1961 and NGC 6753 spirals, in which $\approx 50-70$ % of baryons were found to be missing from the volumes enclosed within R_{vir}. These results were later confirmed by Anderson et al. (2016) and Bogdan et al. (2017) with use of deeper data.

We note however, that there are indications that hot galactic haloes may extend very far out from the host galaxies (e.g., Wakker & Savage 2009; Tumlinson et al. 2011; Stocke et al. 2012; Johnson et al. 2015; Burchett et al. 2019), up to several hundred kpc distances in Milky Way-like galaxies (see e.g., Gupta et al. 2012; Fang et al. 2012). In the case of 3C 273, the sight-line has a $\sim 2.5R_{vir}$ impact parameter with respect to the galaxy G1. Hence, linking the X-ray absorption to the hot halo of G1 would require a substantial CGM, extending far beyond the virial radius. Unfortunately, the available X-ray instrumentation is not capable of providing the information required to determine the mass distribution of hot gas around spirals out to very large radii. (Note that current measurements of the missing baryon budget in spirals, such as those quoted above, are based on parametric profiles, extrapolated from a small fraction of R_{vir} around the central parts of the halo.) Therefore, while we cannot confirm or exclude the possibility that the 3C 273 hot gas absorption would mainly be associated with galaxy G1 (rather than with the filamentary WHIM gas residing in structure F1), this interpretation seems unlikely.

6.3. WHIM gas phases at z=0.09

In this work, we have shown that X-ray grating data yields evidence of hot absorbing gas at $z \approx 0.09$. Tilton et al. (2012), building on the work of Danforth & Shull (2008), Tripp et al. (2008), and Sembach et al. (2001) reported FUV detections of O VI $\lambda\lambda$ 1031.9, 1037.6 Å lines at the corresponding z at 5.0 and 2.8 σ significance levels, indicating a $\log N_{OVI}(\text{cm}^{-2}) = 13.263 \pm 0.110$ column density for O VI. The CIE WHIM model presented in this work only predicts $\sim \frac{1}{10}$ the O VI column density (Table 5) that the FUV data indicate, meaning that a one temperature CIE model is insufficient to explain all the observational results.

At present, observational information on the thermal structures of WHIM absorbers is absent, but, for example, the `EAGLE` (Schaye et al. 2015) simulations indicate that many high column density WHIM absorbers are multi-temperature (e.g., Oppenheimer et al. 2016; Wijers et al. 2019). For such absorbers, multiband analysis may often be required to yield information about the various temperature phases that may co-exist. This is also demonstrated by the CIE WHIM modeling results of this study; despite the fact that the hot phase predicts relatively high N_{OVI}, its absorption imprint cannot be measured in the FUV because of the shallow line profile due to thermal line broadening.

In the absence of detailed knowledge of the $z = 0.09$ absorber's local radiation field, we do not know the precise balance of ionization processes at work. However, if the ionizing radiation field can be predominantly characterized by the typical metagalactic ultraviolet background (UVB; e.g., Haardt et al. 2012), it is unlikely that photoionization is the primary contributor to the observed O VI column densities, as photoionization calculations using a variety of UVB models fail to produce significant O VI column densities (e.g., Tepper-Garcia et al. 2011; Shull et al. 2015; Rahmati et al. 2016). Even in the circumgalactic medium of star-forming L_* galaxies, photoionization is unlikely to drive the production of O VI unless the physical gas densities are extremely low (McQuinn & Werk 2018), or if there has been AGN activity within the last recombination time (Oppenheimer

& Schaye 2013; Segers et al. 2017; Oppenheimer et al. 2018). The ionization of the observed O vi absorber is thus likely driven by collisional processes. Though the frequent association of O vi absorbers with photoionized gas (e.g., lower ionization states of C, N, and Si) suggests that at least some O vi absorbers arise in a non-equilibrium, multiphase gas, we limit our further discussion to the simplified case of collisional ionization equilibrium so that we can derive plausible temperatures for the observed gas.

Assuming the CIE conditions to be valid, the FUV observational results readily set constraints on the gas temperature of the warm absorber. Namely, combining the information of the upper limit on the C iii ion column density ($\log N_{\mathrm{CIII}}(\mathrm{cm}^{-2}) < 12.590$, Tilton et al. 2012) and the lower limit on N_{OVI}, one gets the lower temperature limit if the relative elemental abundances are considered known (because of the C iii, O vi ion fraction T-dependencies). On the other hand, assuming pure thermal line broadening for the O vi line broadening parameter ($b = 22.2 \pm 10.8$ km s^{-1}, Table 1) directly yields an upper temperature limit for absorbing gas.

However, we found that with the help of the X-ray data, these temperature limits can be constrained more accurately. In the two panels of Fig. 8 we present the results obtained with a two phase (warm-hot) CIE absorber model constructed around the relevant information obtained in the X-ray and FUV measurements. In the 2T model (the CIE WHIM model + additional SPEX 'hot'-component for the warm absorber), the hot CIE absorption component was fixed to the best-fit values of the CIE WHIM (Table 5), while the total N_{OVI} ($=N_{\mathrm{OVI}}^{\mathrm{warm}} + N_{\mathrm{OVI}}^{\mathrm{hot}}$) was fixed to the FUV measured value of $\log N_{\mathrm{OVI}}(\mathrm{cm}^{-2}) = 13.263$. We then examined the goodness of fit as a function of warm CIE absorber temperature. We also conducted the same study by omitting the hot WHIM component from the model, to investigate the dependence of the results on the hot CIE component (1T, Fig. 8). We note that in both the 1 and 2T fits, the only free parameter was the warm WHIM temperature T_{warm} (in addition to the absorbed emission model, Sect. 4.3), as $N_{\mathrm{H}}^{\mathrm{warm}}$ is defined by the CIE constraints from the fixed N_{OVI}.

We found that the 2T (and 1T) model yields a global minimum C-statistic in a temperature range matching the FUV derived T limits. More precisely, the 2T fit yielded $T_{\mathrm{warm}} \approx 2.9^{+1.8}_{-1.0} \times 10^5$ K (or $kT_{\mathrm{warm}} \approx 0.025$ keV) with $N_{\mathrm{H}}^{\mathrm{warm}}/N_{\mathrm{H}}^{\mathrm{hot}} \sim 10^{-2}$ (see the left panel in Fig. 8). We note that this solution occurs because towards the lower temperatures, the ratio of N_{OVI} to lower ionization states of oxygen quickly decreases, predicting rise of prominent O iv (blend at $\lambda_0 \approx 22.7$ Å) and O v ($\lambda_0 \approx 22.37$ Å) lines not present in the X-ray spectra (but observed, e.g., in Galactic halo, see Nevalainen et al. 2017). In contrast, when moving towards the higher temperatures, the $\frac{N_{\mathrm{OVII}}}{N_{\mathrm{OVI}}}$ -ratio becomes inconsistent with the X-ray data. The attained 2T solution is in fact the only viable two-phase solution that can simultaneously fulfill both the FUV and X-ray constraints, which can also be understood through the visualization in the right panel of Fig. 8.

Considering the thermal analysis results and the redshift match between the hot and warm absorbers together implies that the FUV and X-ray absorbers are part of the same, multi-temperature structure of intergalactic gas. The redshift match does not necessarily signify strict spatial co-location of the detected gas phases, however, because different thermal phases can occupy spatially distinct physical environments within the same structure. Indeed, recent EAGLE simulations indicate that WHIM structures are often composed of a variety of thermodynamical environments characterized by wide range of densities, temperatures and pressures (e.g., Oppenheimer et al. 2016; Wijers

et al. 2019). Such complexity limits our ability to further examine the absorber properties, by adopting the requirement of pressure equilibrium for different phases for instance, or by means of other similar constraints.

However, combining the information from the FUV and X-ray measurements does give weak constraints on the line-of-sight turbulent velocities v_{turb} associated with the warm WHIM component. Namely, writing the definition of the line Doppler parameter b for v_{turb} we have

$$v_{\mathrm{turb}} = \sqrt{\frac{b^2}{2} - \frac{kT}{m}}, \tag{1}$$

where m is the mass of a given ion, of which we measure a rest-frame spectral linewidth b at gas temperature T. Thus, in the case in hand, the first term inside the square root can be determined by the FUV O vi measurements, whereas the second term can be obtained from the X-ray temperature constraints on the warm WHIM component. (We ignore any hot phase contribution to the FUV O vi line width, since we expect the hot phase to have only $\sim \frac{1}{10} \times$ the O vi column and $\sim 10 \times$ the temperature). Using the obtained values gives us upper limit $v_{\mathrm{turb}} \lesssim 20$ km s^{-1}, or $v_{\mathrm{turb}}/v_{\mathrm{thermal}} \approx 0.5 \pm 0.5$. In order to obtain a lower limit for v_{turb}, more accurate measurements of b would be required. We point out that this method could be applied to constrain v_{turb} for any (collisionally ionized) warm O vi absorbers in lines-of-sight where high-resolution X-ray data with good photon statistics are available.

We will now consider the spectral properties of the BLA lines predicted by the two-phase model to check whether they contradict the non-detection of BLA lines at $z = 0.09$. Richter et al. (2006) found that the BLAs are detectable in STIS data if

$$\frac{N_{\mathrm{HI}}}{b_{\mathrm{HI}}} \gtrsim \frac{3 \times 10^{12}}{(\mathrm{S/N})}\, \mathrm{cm}^{-2}\, (\mathrm{km\, s}^{-1})^{-1}, \tag{2}$$

where (S/N) denotes the signal-to-noise ratio per spectral resolution element at the location of the BLA. We examine the detectability of the predicted BLAs using the Williger et al. (2010) quoted sensitivity limit for STIS spectral data at the 3C 273 sight-line ($\log N_{\mathrm{HI}}/b_{\mathrm{HI}} \approx 10.9$ at $z \approx 0.09$). According to the best-fit 2T model, the two BLAs are characterized by $b_{\mathrm{HI}}^{\mathrm{warm}} \approx 69$ km s^{-1}, $N_{\mathrm{HI}}^{\mathrm{warm}} \approx 10^{11.3} \times Z_{\odot}/Z_{\mathrm{warm}}$ cm^{-2} and $b_{\mathrm{HI}}^{\mathrm{hot}} \approx 223$ km s^{-1}, $N_{\mathrm{HI}}^{\mathrm{hot}} \approx 10^{12.0} \times Z_{\odot}/Z_{\mathrm{hot}}$ cm^{-2} (here we have neglected the non-thermal line broadening, which would effectively decrease the line detectability). The detection criterion in Eq. 2 may then be written as $N_{\mathrm{HI}}^i/b_{\mathrm{HI}}^i \times 10^{-10.9} \gtrsim Z^i/Z_{\odot}$, which yields metallicity limits $Z_{\mathrm{warm}} \approx 0.04 \times Z_{\odot}$ and $Z_{\mathrm{hot}} \approx 0.06 \times Z_{\odot}$, above which the lines are undetectable. Therefore neither of the phases produces detectable BLAs at the expected metallicity range of filamentary WHIM, $Z = 0.1 - 0.4 \times Z_{\odot}$ (Martizzi et al. 2019), and the non-detectability is also consistent with our weak limit on the hot phase metallicity, $Z_{\mathrm{hot}} \sim 10^{-1}$ (see Sect. 6.1.1).

7. Comparison to Simulations

In Sect. 6.1.1 we showed that the FUV and X-ray absorption at $z \approx 0.09$ can originate from WHIM located in a large scale filamentary structure (of the Cosmic Web). Then, in Sect. 6.2 we found that the nearest detected galaxy to the absorber is unlikely to produce the measured absorption. However, it is still possible that at the location of the absorber there are galaxies fainter than the SDSS detection limit, which could produce the measured level of O vi. In this case, only the X-ray lines would originate from the intergalactic medium in the filament.

In order to gain more insight of the physics of the co-located FUV and X-ray absorbers, we investigated the `EAGLE` cosmological, hydrodynamical simulations (Schaye et al. 2015, Crain et al. 2015, McAlpine et al. 2016). Given the various possibilities for the environment of the $z \approx 0.09$ absorbers, we did not attempt to separate the haloes and the filaments when extracting the simulated data for this study. In this section, we summarize the observable properties of spatially co-located hot (O vii, O viii and Ne ix), and warm WHIM (O vi) absorbers in `EAGLE`, and compare these predictions to our measurements.

7.1. EAGLE simulation

The code for the `EAGLE` simulations is a modified version of `GADGET`3 (last described in Springel 2005). It uses a TREE-PM scheme to calculate gravitational forces. One of the modifications made to `GADGET`3 is the use of a different hydrodynamics solver: `EAGLE` uses a smoothed particle hydrodynamics (SPH) implementation known as `ANARCHY` (Schaye et al. 2015, Schaller et al. 2015). Cosmological parameters were taken from Planck Collaboration et al. (2014).

Gas cooling is implemented per element as described by Wiersma et al. (2009), using the abundances of 11 elements tracked in the simulation. Ionization equilibrium with collisional processes and photo-ionization by a Haardt & Madau (2001) UV and X-ray background is assumed. Since the particle mass of the simulations is $\approx 2 \times 10^6 \, M_\odot$, we cannot resolve the formation of and feedback (stellar winds and supernovae) from individual stars, accretion disks, jets, etc. in AGN. Therefore, star formation and stellar and AGN feedback on the mass scales we can resolve are implemented using subgrid models. The feedback models have free parameters, which were chosen by calibrating them to reproduce the $z = 0.1$ galaxy stellar mass function, the relation between black hole mass and galaxy mass, and reasonable galaxy sizes. We use the $100^3 \, \mathrm{Mpc}^3$ simulation volume (L100N1504) at $z = 0.1$, which was run with the standard `EAGLE` subgrid parameters (the Reference model).

We compute column densities as in Wijers et al. (2019). In short, we assume the gas is in collisional and photo-ionisation equilibrium with the Haardt & Madau (2001) UV/X-ray background at $z = 0.1$. We then use the gas temperatures, densities, and oxygen mass fractions from the simulation to compute the number of ions in long, thin columns along the line of sight. The columns are thin enough that the column densities at the values we observe are converged. Their line of sight length was chosen to be 6.25 comoving Mpc, which corresponds to $404 \, \mathrm{km \, s^{-1}}$ (rest-frame) in velocity space, ignoring peculiar velocities, or $\Delta z = 0.0015$. When comparing temperatures for the different ions, we measure ion-weighted temperatures in the same columns. We define counterpart column densities to be column densities measured in the same columns for different ions. Since we define our simulated absorbers by these fixed boxes, our column density and counterpart determinations from `EAGLE` are only an approximation of what an observer would measure in an `EAGLE` universe. The redshift range in these slices does roughly match the difference between the O vi and X-ray centroids, although the z uncertainty is large in the X-ray. While we did not impose any direct filament environment selection criteria on the `EAGLE` data, we note that concentrating on the densest hot WHIM, we are approximately focusing on locations close to the filament axes, as indicated by the cosmological simulations such as the `EAGLE` and `IllustrisTNG` (see Nelson et al. 2018a).

7.2. Results

In Fig. 9, we investigate what sort of X-ray counterparts we would expect to find for the O vi absorber at $z = 0.09$, based on its column density. In `EAGLE`, such an absorber can have a broad range of O viii and Ne ix column densities, but the absorption in the two X-ray lines is strongly correlated. The measured X-ray column densities are large compared to the predictions, but not unreasonably so, especially considering the minimum detectable absorption and the non-detection of X-ray counterparts for the $z = 0.12$ O vi absorber. The CIE WHIM model column densities agree better with the `EAGLE` predictions than the 'slab' column densities, but both are within $1 - 2\sigma$ of the region where 90 % of absorbers consistent with the observed O vi column densities lie in `EAGLE`, if the observed upper limit on O vii is ignored (left panel of Fig. 9). Including the 'slab' model O vii upper limit means the O viii/Ne ix absorption measured with the 'slab' model agrees slightly less well with `EAGLE` (right panel of Fig. 9). However, given the $\sim 10^{15} \, \mathrm{cm^{-2}}$ detection limit for O viii and Ne ix, any of the most likely $\sim 90\%$ of O vi, O vii upper limit counterparts would be undetectable with current instrumentation. Considering this selection effect, and the non-detection of a hot counterpart for the O vi absorber at $z = 0.12$ (characterized with similar N_{OVI} to $z = 0.09$ absorber, Table 1), we find that the FUV and X-ray ion column density measurements are generally consistent with the `EAGLE` predictions.

Then we ask the question of whether the `EAGLE` simulations support the 2-temperature solution we obtained with the X-ray and FUV spectroscopy for the absorber at $z = 0.09$. To answer this, we performed a test where we compared our 2T-fit temperatures T_{warm} and T_{hot} (Sect. 6.3) with corresponding quantities obtained from the simulation: T_{OVI} and T_{OVIII} ion mass weighted temperatures. For the comparison, we had to choose a subsample of the simulations which represents the conditions of the $z = 0.09$ absorber. Since we were testing the temperatures, we obviously did not use the temperatures to select the subsample. Instead, we imposed the measured constraints on the absorber's O vi (Tilton et al. 2012), O vii, O viii and Ne ix ('slab' constraints) column densities as the selection criteria when extracting the simulation data.

We illustrate the result of this study in Fig. 10, where we examine the effect of different N_{ion} constraints on `EAGLE` distribution one by one. Adding just the O vi constraint readily shows that O viii and Ne ix often trace gas that is at different temperatures than the O vi-rich phase (top left panel). We find that adoption of the O vii upper limit does not strongly constrain the number of absorption systems in `EAGLE` (top right panel), whereas the opposite is true for O viii and Ne ix, which strongly limit the temperature phase distribution of the absorption systems (bottom panels). Indeed, when all the N_{ion} measurement constraints are applied, the necessity of 2T conditions emerges in `EAGLE`. This subsample behaves well in the T_{OVI}-T_{OVIII} plane, forming a regular, relatively narrow region. Notably, we find that absorption systems with column densities like those of the $z = 0.09$ absorber tend to have O vi and O viii temperatures that agree well with the 2T CIE temperatures (bottom right panel). Thus, we find that the 2T CIE model is well supported by the simulations, which validates the use of CIE modeling adopted in this work.

8. Discussion

In this work we search for the absorption imprints of hot WHIM at the redshifts of warm intergalactic (O vi) absorbers. We examine the X-ray data in a sight-line which provides one of the
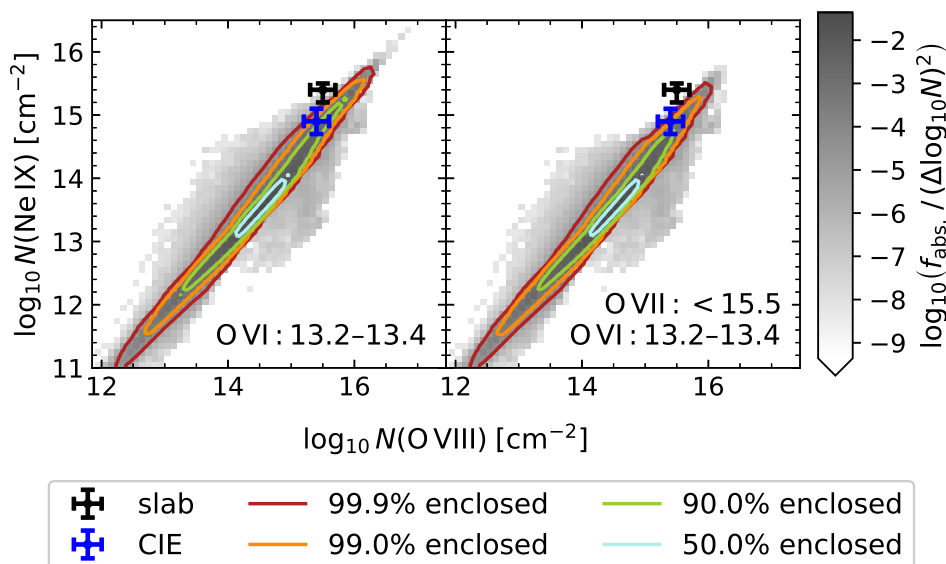
Fig. 9. The distribution of O viii and Ne ix column densities in counterparts to O vi absorbers (grayscale and contours) according to the EAGLE simulation, compared to the measured column densities at $z = 0.09$ for the CIE and slab models. In the left panel we show counterparts to O vi absorbers with column densities of $10^{13.2}$–$10^{13.4}$ cm^{-2}, which is roughly the $\pm 1\sigma$ range for the FUV absorber of Tilton et al. (2012). In the right panel, we show the subset of O vi counterparts with an O vii column density in agreement with the upper limit measured with the slab model. The contours enclose different fractions of the counterparts, as indicated in the legend, while the grayscale shows the fraction of all EAGLE absorbers satisfying the indicated constraints. Although most EAGLE O vi absorbers have weaker (and hence undetectable) associated Ne ix and O viii absorption than observed at $z = 0.09$ (but consistent with the non-detection for the $z = 0.12$ O vi absorber), both the 'slab' and CIE measuremets are consistent with EAGLE at the $\approx 1 - 2\sigma$ level. The O vii upper limit does not affect the distribution much.

highest level photon statistics currently available, including observational data from 5 different high spectral-resolution X-ray instruments. Our analysis yielded a positive indication at one out of two examined O vi redshifts. However, given that we only analyzed two O vi absorbers, the uncertainty in the observational detection rate is large and one cannot draw a general conclusion from such small number statistics. Indeed, EAGLE predicts only an 11 % chance of finding an O viii counterpart as strong as we found (CIE model) to at least one of the two examined O vi absorbers, indicating that the observational detection rate was driven by luck.

Based on this study, we are able to make a few general remarks regarding FUV-guided searches for hot WHIM. First, two search criteria (as defined in Sect. 4.2) were initially set in order to filter out all but the most promising FUV absorber redshifts for the X-ray analysis. In hindsight it seems, however, that the BLA criterion might have only limited use for this. Namely, considering the inevitably large b_{HI} associated with gas phases not producing a detectable O vi signal in the FUV yet still producing strong lines in X-ray, such BLA detections seem unlikely. This is because robust detections of broad HI lines require high N_{HI}, in which cases the absorber metallicities should be low given the current upper limits on WHIM ionic columns, but still high enough to enable X-ray detection. Such special requirements for the environment likely mean the number of X-ray absorbers only traceable with BLAs is small.

Second, O vii is often expected to be the most prominent X-ray detectable ion species to accompany O vi absorbers, which is a justified assumption given the Oxygen ion fraction temperature dependencies. However, the evidence presented in this work demonstrates that O vi absorbers can also be used to reveal locations of hot X-ray absorbers whose O vii signal is below de-

tectability, or in other words, when the circumstances are such that the two bands would effectively detect thermally distinct gas phases. As the combination of low O vi ion fractions and the broad line shapes of the hot WHIM phases significantly reduces the O vi FUV detectability, the FUV measured b_{OVI} should not been interpreted as a direct proxy for the (maximum) temperature of the absorber. Rather, b_{OVI} may often be merely a property of the most easily detectable gas phase within an otherwise thermally complex structure, as may also be inferred from the top panels of Fig. 10.

9. Conclusions

In this work we examined the O vi detection driven method to find missing baryons in the hot WHIM phase. We analyzed the available high-resolution spectral data of XMM-*Newton* RGS, *Chandra* LETG and MEG for the quasar 3C 273, which is one of the brightest quasars in X-ray. We searched for the hot WHIM absorption signatures at the two redshifts where O vi absorbers have been significantly detected in the FUV band. Our main results include:

1. At one of the FUV determined redshifts, $z = 0.09017$, spectral analysis with a line absorption model yields two X-ray line candidates whose centroid wavelengths match the Ne ix Heα ($W_{rest-frame} = 2.7 \pm 0.9$ mÅ, confidence level 2.9 σ) and O viii Lyα ($W_{rest-frame} = 4.3 \pm 1.6$ mÅ, 2.6 σ) lines. These two ion species are prominent in the same temperature range ($T \approx 10^{6-6.5}$ K), thus yielding 3.9 σ combined (quadratically summed) confidence level for the hot phase lines.
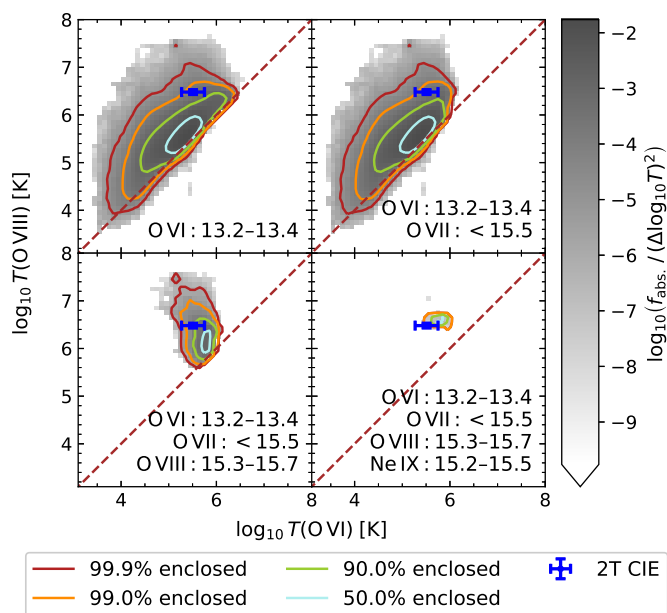
Fig. 10. The distribution of O VI- and O VIII-weighted temperatures in counterparts to O VI absorbers (grayscale and contours) according to the `EAGLE` simulation, compared to the best-fit temperatures at $z = 0.09$ for the 2-temperature CIE model (warm and hot phase, respectively). From left to right, top to bottom, we show how constraints on the column densities of different ions from the 'slab' model affect the temperatures of O VI and O VIII absorbers in `EAGLE`. Column density ranges are shown in units of $\log_{10}$ cm^{-2} for the different ions. The O VI constraints are from Tilton et al. (2012). The contours enclose different fractions of the absorbers in each column density selection, as indicated in the legend, while the grayscale shows the fraction of all `EAGLE` absorbers satisfying the indicated constraints. The brown dashed line indicates where the temperatures are equal. Most absorbers are multiphase and the 2T CIE model is consistent with `EAGLE`.

2. Examining the spectral characteristics at the same redshift assuming collisional ionization equilibrium (CIE) for the absorber yields $kT = 0.26 \pm 0.03$ keV and $N_H = 1.3^{+0.6}_{-0.5} \times 10^{19} Z_\odot/Z$ cm^{-2} for the absorbing medium. The column densities of O VIII and Ne IX predicted by this model ($\log N_{O\,VIII}$(cm^{-2}) $= 15.4 \pm 0.2$, $\log N_{Ne\,IX}$(cm^{-2}) $= 14.9 \pm 0.2$) are in close agreement with those measured phenomenologically from the line flux ($\log N_{O\,VIII}$(cm^{-2}) $= 15.5 \pm 0.2$, $\log N_{Ne\,IX}$(cm^{-2}) $= 15.4^{+0.1}_{-0.2}$), indicating the hot phase is well described by the CIE model.

3. The thermal analysis implies a multi-temperature structure for the $z \approx 0.09$ absorber, with dominant temperature components of $T_{warm} \approx 3 \times 10^5$ K and $T_{hot} \approx 3 \times 10^6$ K, and hydrogen column density ratio $N_H^{warm}/N_H^{hot} \sim 10^{-2}$, when assuming CIE conditions and identical metallicities for both phases (Fig. 8). These results match the `EAGLE` hydrodynamical simulation temperature predictions for co-spatial WHIM absorbers characterized with ion column densities matching the FUV and X-ray measurements (lower right panel in Fig. 10).

4. SDSS galaxy distribution modeling detected a large scale filament of galaxies crossing the sight-line at the location matching the FUV and X-ray absorbing gas (Fig. 7). The total WHIM hydrogen column density at the 3C 273 sight-line through the filament was estimated to be $N_H \sim 2 \times 10^{19}$

cm^{-2}. Associating this value with the results of the X-ray analysis yields an absorber metallicity $Z \sim 10^{-1} \times Z_\odot$, which is in the range expected for the WHIM. Combining our results hence supports the hypothesis that the X-ray and FUV absorption signals relate to a filamentary WHIM structure intersecting the 3C 273 sight-line at $z \approx 0.09$.

5. We found no indications of X-ray absorbing gas at the other of the two examined O VI redshifts, $z = 0.12005$. Since this absorber is characterized by N_{OVI} similar to the absorber at $z = 0.09017$, we have a nominal 50 % (1 of 2) detection-rate for X-ray absorbing counterparts to N_{OVI}(cm^{-2}) $\approx 13.2 -$ 13.4 FUV absorbers at the examined sight-line. By comparison, `EAGLE` predicts 11 % likelihood to find at least one $\log N_{OVIII}$(cm^{-2}) ≥ 15.4 counterpart per two randomly selected O VI absorbers in the coincident N_{OVI} range. However, regarding future observations with X-ray instruments capable to detect $\log N_{OVIII}$(cm^{-2}) ≥ 15.0 signals, such as the Athena X-IFU, the same likelihood is already 29 %. This reflects the potential in utilizing the information on O VI absorbers in finding missing baryons in hotter, X-ray absorbing phase.

References

Anderson, M. E., Churazov, E., & Bregman, J. N. 2016, MNRAS, 000, 449
Barret, D., Lam Trong, T., den Herder, J. W., et al. 2016, Space Telescopes and Instrumentation2016: Ultraviolet to Gamma Ray, 9905, 99052F
Bogdan, A., Bourdin, H., Forman, W. R., et al. 2017, ApJ, 850, 98
Bogdan, A., Forman, W. R., Vogelsberger, M., et al. 2013, ApJ, 772, 97
Bonamente, M. 2017, Statistics and Analysis of Scientific Data (Springer, Graduate Texts in Physics, Second Edition)
Bonamente, M., Ahoranta, J., Tilton, E., Tempel, E., & Morandi, A. 2017, MNRAS, 469, 3984
Bonamente, M., Nevalainen, J., Tilton, E., et al. 2016, MNRAS, 457, 4236
Buote, D. A., Zappacosta, L., Fang, T., et al. 2009, ApJ, 695, 1351
Burchett, J. N., Tripp, T, M., Prochaska, J. X., Werk, J. K., et al. 2019, ApJ, 877, L20
Cartledge, I. B., Lauroesch, J. T., Meyer, D. M., & Sofia, U. J. 2004, ApJ, 613, 1037
Cash, W. 1979, ApJ, 228, 939
Cen, R. & Ostriker, J. P. 1999, ApJ, 514, 1
Crain, R. A., Schaye, J., Bower, R. G., et al. 2015, MNRAS, 450, 1937
Danforth, C. W., Keeney, B. A., Tilton, E. M., et al. 2016, ApJ, 817, 28
Danforth, C. W. & Shull, J. M. 2008, ApJ, 679, 194
Davé, R., Hernquist, L., Katz, N., & Weinberg, D. H. 1999, ApJ, 511, 521
de Vries, C. P., den Herder, J. W., Gabriel, C., et al. 2015, å, 573, A128
Fang, T., Bryan, G. L., & Canizares, C. R. 2002, ApJ, 564, 604
Fang, T., Bullock, J., & Boylan-Kolchin, M. 2012, ApJ, 762, 20
Fang, T., Sembach, K. R., , & Canizares, C. R. 2003, ApJL, 586, 49
Gehrels, N. 1986, ApJ, 303, 336
Gupta, A., Mathur, S., Krongold, Y., et al. 2012, ApJL, 756, L8
Haardt, F., , & Madau, P. 2012, ApJ, 746, 125
Haardt, F. & Madau, P. 2001, in Clusters of Galaxies and the High Redshift Universe Observed in X-rays, ed. D. M. Neumann & J. T. V. Tran
Johnson, S. D., Chen, H.-W., & Mulchaey, J. S. 2015, Monthly Notices of the Royal Astronomical Society, 449, 3263–3273
Kaastra, J., Finoguenov, A., Nicastro, F., Branchini, E., et al. 2013, arxiv:1306.2324
Kaastra, J. S., de Vries, C. P., Steenbrugge, K. C., et al. 2011, A& A, 534, 37
Kooistra, R., Silva, M. B., & Zaroubi, S. 2017, MNRAS, 468, 857
Kovacs, O. E., Bogdan, A., Smith, R. K., Kraft, R. P., & Forman, W. R. 2019, ApJ, 872, 83
Licquia, T. C., Newman, J. A., & Brinchmann, J. 2015, ApJ, 809, 96
Liivamagi, L. J., Tempel, E., & Saar, E. 2012, A&A, 539, A80
Lodders, K., Palme, H., & Gail, H.-P. 2009, Landolt-Börnstein - Group VI Astronomy and Astrophysics, 712–770

Martizzi, D., Vogelsberger, M., Artale, M. C., Haider, M., et al. 2019, MNRAS, 486, 3766–3787

McAlpine, S., Helly, J. C., Schaller, M., et al. 2016, Astronomy and Computing, 15, 72

McQuinn, M. & Werk, J. K. 2018, ApJ, 852, 33

Nelson, D., Pillepich, A., Springel, V., Weinberger, R., & et al. 2018a, MNRAS, 477, 1206

Nelson, N., Kauffmann, G., Pillepich, A., et al. 2018b, arxiv:1712.00016

Nevalainen, J., Tempel, E., Ahoranta, J., Liivamagi, L. J., et al. 2019, A& A, 621, 88

Nevalainen, J., Tempel, E., Liivamagi, L. J., et al. 2015, A&A, 583, A142

Nevalainen, J., Wakker, B., Kaastra, J., Bonamente, M., et al. 2017, A &A, 605, 47

Nicastro, F., Kaastra, J., Krongold, Y., et al. 2018, Nature, 558, 406

Nicastro, F., Krongold, Y., Fields, D., et al. 2010, ApJ, 715, 854

Nicastro, F., Krongold, Y., Mathur, S., & Elvis, M. 2017, Astronomische Nachrichten, 338, Iss. 2-3, 281

Oppenheimer, B. D., Crain, R. A., Schaye, J., et al. 2016, MNRAS, 460, 2157

Oppenheimer, B. D. & Schaye, J. 2013, MNRAS, 434, 1063

Oppenheimer, B. D., Segers, M. C., Schaye, J., Richings, A. J., & Crain, R. A. 2018, MNRAS, 474, 4740

Persic, M. & Salucci, P. 1992, MNRAS, 258, 14

Planck Collaboration, Ade, P. A. R., Aghanim, N., et al. 2014, A&A, 571, A1

Rahmati, A., Schaye, J., Crain, R. A., et al. 2016, MNRAS, 459, 310

Rasmussen, A. P., Kahn, S. M., Parels, F., et al. 2007, ApJ, 656, 129

Ren, B., Fang, T., & A., B. D. 2014, ApJ, 782, L6

Richter, P., Savage, B. D., Sembach, K. R., & Tripp, T. M. 2006, A& A, 445, 827

Savage, B. D., Lu, L., Weymann, R. J., Morris, S. L., & Gilliland, R. L. 1993, ApJ, 404, 124

Schaller, M., Dalla Vecchia, C., Schaye, J., et al. 2015, MNRAS, 454, 2277

Schaye, J. 2001, ApJ, 559, 507

Schaye, J., Crain, R. A., Bower, R. G., Furlong, M., et al. 2015, MNRAS, 446, 521

Schmidt, M. 1963, Nature, 197, 1040

Segers, M. C., Oppenheimer, B. D., Schaye, J., & Richings, A. J. 2017, MNRAS, 471, 1026

Sembach, K. R., Howk, J. C., Savage, B. D., Shull, J. M., & Oegerle, W. R. 2001, ApJ, 561, 573

Shull, M. J., Moloney, J., Danforth, C. W., & Tilton, E. M. 2015, ApJ, 811, 3

Shull, M. J., Smith, B. D., & Danforth, C. W. 2012, ApJ, 759, 23

Springel, V. 2005, MNRAS, 364, 1105

Stocke, J. S., Keeney, B. A., Danforth, C. W., et al. 2012, ApJ, 763, 148

Tempel, E., Stoica, R. S., Kipper, R., & Saar, E. 2016, Astronomy and Computing, 16, 17

Tempel, E., Stoica, R. S., Martinez, V. J., et al. 2014a, MNRAS, 438, 3465

Tempel, E., Tamm, A., Gramann, M., et al. 2014b, A&A, 566, A1

Tempel, E., Tuvikene, T., Kipper, R., & Libeskind, N. I. 2017, A&A, 602, A100

Tepper-Garcia, T., Richter, P., Schaye, j., et al. 2011, MNRAS, 413, 190

Tepper-Garcia, T., Richter, P., Schaye, J., et al. 2012, MNRAS, 425, 1640

Tilton, E., Danforth, C. W., Shull, M. J., & Ross, T. L. 2012, ApJ, 759, 112

Tripp, T. M., Savage, B. D., & Jenkins, E. B. 2000, ApJ, 534, L1

Tripp, T. M., Sembach, K. R., Bowen, D. V., et al. 2008, ApJS, 177, 39

Tumlinson, J., Thom, C., Werk, Prochaska, T. M., & Tripp, T. M. 2011, Science, 334, 948

Wakker, B. P. & Savage, B. D. 2009, ApJS, 182, 378

Wiersma, R. P. C., Schaye, J., & Smith, B. D. 2009, MNRAS, 393, 99

Wijers, N., Schaye, J., Oppenheimer, B. D., Crain, R. A., & Nicastro, F. 2019, MNRAS, 488, 2947

Williger, G. M., Carswell, R. F., Weymann, R. J., et al. 2010, MNRAS, 405, 1736

Willingale, R., Starling, R. L. C., Beardmore, A. P., Tanvir, N. R., & O'Brien, P. T. 2013, MNRAS, 431, 394

Yao, Y., Tripp, T. M., Wang, Q. D., Danforth, C. W., et al. 2009, ApJ, 697, 1784